Key Points:

- First fluid gold concentrations (0.045 ± 0.024 µg/g) measured from an economic, Meguma-type metasediment-hosted gold deposit
- Fluid Au, S, As, W, and B concentrations comparable to Alpine and Variscan metamorphic fluids hosted in uneconomic, Au-poor vein systems
- Gold and carbonaceous matter are coeval and co-distributed in flysch wallrocks and vein laminae

Supporting Information:

Supporting Information may be found in the online version of this article.

Correspondence to:

M. J. Kerr,
mitchell.kerr@smu.ca

Auriferous Fluid Evolution and the Role of Carbonaceous Matter in a Saddle-Reef Gold Deposit: Dufferin Deposit, Meguma Terrane, Nova Scotia, Canada

Mitchell J. Kerr[1,2] , **Jacob J. Hanley[1]**, **Daniel J. Kontak[2]** , **Preetysha Ramlochund[1]**, and **Zoltán Zajacz[3]**

[1]Department of Geology, Saint Mary's University, Halifax, NS, Canada, [2]Harquail School of Earth Science, Laurentian University, Sudbury, ON, Canada, [3]Department of Earth Science, University of Toronto, Toronto, ON, Canada

Abstract The metaturbidite-hosted, ~380 Ma Dufferin gold deposit, Meguma terrane, northeastern Appalachian Orogen (Nova Scotia, Canada) is an orogenic gold deposit with mineralized saddle reef-type quartz veins hosted by metasandstones and black slates in a tightly folded anticline. Together with native gold inclusions, genetically related hydrothermal carbonaceous material (CM) in veins occurs as pyrobitumen in cavities and along fractures/grain boundaries proximal to vein contacts and wallrock fragments. Integrating several microanalytical methods we document the precipitation of gold via coupled fluid-fO_2 reduction (via interaction with CM) and pH increase. These changes in fluid chemistry destabilized gold bisulfide complexes, leading to efficient Au precipitation from a gold-undersaturated (0.045 ± 0.024 ppm Au; 1σ; $n = 58$ fluid inclusions) aqueous-carbonic fluid (H_2O-NaCl-$CO_2 ± N_2 ± CH_4$). The proposed mineralization mechanism is supported by: (a) a complementary decrease in Au and redox-sensitive semimetals (As, Sb), and increase in wall rock-derived elements (i.e., Mg, K, Ca, Sr, Fe) concentrations in fluid inclusions with time; (b) a corresponding decrease in the X_{CO_2}, consistent with CO_2 removal via reduction/respeciation and late carbonate precipitation; and (c) gold embedding in, or on, the surface of CM inside mineralized cavities and fractures. Despite mineralizing fluids transporting low concentrations of Au far from saturation, precipitation of gold was locally evidently high where such fluids interacted with CM, contributing to the overall gold endowment of Meguma deposits. This work re-emphasizes CM as a potential prerequisite for efficient gold precipitation within the overall genetic model for similar orogenic metasedimentary settings globally where the presence and/or role of CM has been documented.

Plain Language Summary The Dufferin gold deposit in Nova Scotia, Canada, formed ~380 million years ago within metamorphosed sedimentary rocks called the Meguma Group. The deposit contains gold-bearing quartz veins sandwiched between layers of tightly folded rocks. This study focused on unraveling the mechanisms behind some of the gold deposition within this deposit, specifically where associated with carbonaceous matter (CM). We found a close association between gold and CM, which represents organic matter preserved in the rocks. CM is abundant within small cavities throughout the quartz veins that also contain appreciable gold occurring as microscopic particles in the CM. By using a variety of analytical techniques, we determined that efficient gold mineralization occurred in response to specific chemical changes to the gold-carrying fluid, including a decrease in the oxidation potential and a decrease in the acidity of the fluid through interaction with the CM-rich rocks. Such changes to the fluid caused gold to become insoluble and form particles that were deposited in the rocks and vein material. Importantly, despite the fluid having a low concentration of dissolved gold, it exhibited a remarkable ability to deposit significant quantities of the precious metal, underscoring the important role of CM in facilitating efficient gold precipitation from fluids.

1. Introduction

The formation of orogenic gold deposits (OGD) requires the critical marriage of a structurally accessible Au source reservoir, ideal physicochemical characteristics for a fluid to complex and transport Au, and one or more efficient precipitation mechanism(s) (e.g., Gaboury, 2019 and references therein). A combination of voluminous and prolonged fluid flux into structurally overprinted, multiphase deformation zones characterizes OGD settings (Dubé & Gosselin, 2007; Goldfarb et al., 2005), and significantly risk compromising the preservation of fluid inclusions (i.e., via post-entrapment modification and leakage, or fluid loss during dissolution-recrystallization processes), which represent the only direct evidence of the former mineralizing fluid(s) (e.g., Kontak &

Tuba, 2017; Ridley & Diamond, 2000; Ridley & Hagemann, 1999). These impediments can have a notable impact on the acquisition of robust fluid inclusion data and the identification of the causative factors that controlled Au solubility and subsequent precipitation (e.g., fluid interaction with carbonaceous material, fluid mixing, boiling/immiscibility, wall-rock reactions, etc.). Therefore, this aspect must be considered when trying to characterize the evolution of fluids via fluid inclusions in OGD.

Additionally, as observed in many other OGD in the Meguma terrane (e.g., Horne & Culshaw, 2001; Kontak & Horne, 2010; Sangster & Smith, 2007), the auriferous saddle-reef veins at Dufferin are localized to anticlinal fold crests where carbonaceous material (CM)-bearing black slates (≥1% organic C; Bierlein & Smith, 2003) are in contact with metasandstones which together define the Bouma sequences characteristic of these metaturbidite sequences. As such, in addition to fluid inclusion preservation, this setting affords the opportunity to investigate the role of CM with respect to gold mineralization and fluid evolution. The occurrence and relevance of CM has been noted in other sedimentary rock-hosted and/or associated gold-mineralized systems globally (e.g., Witwatersrand, South Africa: Fuchs et al., 2017; Parnell, 1996; the Kupferschiefer, Poland: Oszczepalski et al., 2011; Cosmo Howley gold deposit, Northern Australia: Matthäi et al., 1995; Western Lachlan Orogen, Victoria, Australia: Bierlein et al., 2001; Macraes Gold Mine, Otago Schist, New Zealand: Craw, 2002; Pitcairn et al., 2006; Hoyle Pond deposit, Abitibi greenstone belt, Canada: Dinel et al., 2008; Ashanti gold belt, Ghana: Berge, 2011; Table 1). These studies speculate that the CM played a key role in ore genesis as a fluid reductant and redox buffer, a source of critical volatile species (CO_2, H_2S) and metals (As-Au), a lubricant for shear/fault systems, and/or a Au adsorbent (Oszczepalski et al., 2011; Tan et al., 2005; Vilor, 1983; Williams-Jones et al., 2009).

At the metaturbidite-hosted Dufferin gold deposit in the Meguma terrane of the northern Appalachian Orogen (Nova Scotia, Canada), intermittent underground mining (2003–2018) provided excellent access to numerous vein exposures (Horne & Jodrey, 2001). In several of the upper saddle-reef veins of the stacked sequence, we observed vugs/cavities occluded by undeformed quartz crystals containing exceptionally well-preserved and unusually large (i.e., 50 to ≥200 μm) fluid inclusions; these provided a rare opportunity to fully characterize the composition and evolution of hydrothermal fluids thought to be coeval with gold formation. In particular, the size of the fluid inclusions in the quartz is advantageous as this allows for less ambiguous observations of phase changes during microthermometry, an issue that commonly limits studies of fluid inclusions in OGD, and the application of more comprehensive analytical protocols rarely applied to OGD. For example, the atypically large size of the inclusions affords low detection limits for specific analytical methods (e.g., Au detection and quantification by laser ablation inductively-coupled plasma mass spectrometry [LA-ICP-MS]), providing the opportunity to fully characterize the fluids with respect to their solute and volatile chemistry. The acquired fluid inclusion data are integrated with characterization of the CM via scanning electron microscope energy dispersive spectroscopy (SEM-EDS) and laser Raman microspectroscopy (LRM), along with mineral paragenesis and isotopic ($\delta^{13}C$) considerations to track the chemical evolution of the mineralizing fluid at the deposit site and its potential source. As such, this study presents one of the few examples where measured Au concentrations in aqueous-carbonic fluids in an OGD can be directly related to CM in a flysch-hosted gold system.

2. Geologic Setting of the Dufferin Gold Deposit

The Lower Paleozoic metasedimentary rock-hosted Dufferin deposit, located ∼100 km east of Halifax, occurs in the Meguma terrane of southern Nova Scotia, Canada (Figure 1a inset), which is one of several terranes that make up the northeastern Appalachian collage. This terrane was dextrally docked to the adjacent Avalon terrane along the east-west trending Cobequid-Chedabucto Fault Zone (CCFZ in Figure 1a) as part of the Neoacadian Orogeny (Murphy et al., 2011; van Staal, 2007). The terrane is dominated by a thick sequence (12 km) of Cambrian to Ordovician turbiditic, variably carbonaceous (e.g., <1–10% organic carbon; Graves & Zentilli, 1988; Waldron, 1992) metasedimentary rocks of the Goldenville and Halifax groups that are disconformably overlain by Silurian to Early Devonian metasedimentary and metavolcanic rocks of the Rockville Notch Group (White et al., 2012). This sequence was metamorphosed (lower greenschist but locally to amphibolite facies) and deformed (northeast trending open- to closed, upright folds) from ∼410 to 380 Ma (Hicks et al., 1999; Kontak et al., 1998; Morelli et al., 2005). Subsequent emplacement of several large meta- to peraluminous granitoids and minor mafic bodies from ∼370–380 Ma occurred across the terrane (Bickerton et al., 2022; Clarke et al., 1997; Kontak et al., 2004) with related contact aureoles indicating emplacement at pressures of ca. 3–4 kbars (Jamieson

Table 1
Occurrences and Influence of Carbonaceous Material (CM) in Various Au-Mineralized Settings Globally

Deposit	Reference(s)	CM type	CM occurrence	Au occurrence	CM timing wrt. Au	Role of CM
Con & Giant deposits, Yellowknife district, NWT, Canada	Padgham (1986); van Hees et al. (1999); Shelton et al. (2004)	Not explicitly stated; presumably bitumens and pyrobitumens	Metaturbidites	Disseminated with sulfides; minor auriferous Qtz veining	pre	Devolatilization of CM-bearing rocks generated CO_2-rich fluid important for Au mobilization.
Kupferschiefer, Poland	Oszczepalski et al. (2011)	Bitumens, pyrobitumen, vitrinite, liptinite	Shale and carbonate units	Disseminated with sulfides	pre (syn oxidation/pyrolysis)	Redox interface trap. Ore fluid reductant
Cosmo Howley deposit, N. Australia	Matthäi et al. (1995)	Not explicitly stated; presumably bitumens and pyrobitumens	Pelitic metasedimentary units	Auriferous Qtz veins	pre (syn oxidation/pyrolysis)	Reduction of ore fluid by carbonaceous metasediments or fluid mixing by reduced wallrock-equilibrated fluids
Western Lachlan Orogen, Victoria, Australia	Bierlein et al. (2001)	Amorphous bitumens and pyrobitumens; minor graphite	Black shales	Auriferous Qtz veins; minor disseminations in wallrocks	pre (syn oxidation/pyrolysis)	Minor chemical influence by CM at deposit-scale; local reduction of ore fluid by shales or fluid mixing by reduced wallrock-equilibrated fluids; potential surface fixation reactions
Yilgarn Block deposits, W. Australia	McNaughton et al. (1990); Steadman et al. (2013)	Kerogen (biogenic carbon)	Black shales	Auriferous Qtz veins and breccias; disseminated with sulfides in vein alteration halos	pre	Contribution of $CO_2 \pm H_2S \pm$ As-Au to ore fluid through decarbonation of wallrocks
Macraes deposit, New Zealand	Craw (2002); Pitcairn et al. (2005, 2006); Upton and Craw (2008)	Hydrothermal graphite	Shear zones in schists	Auriferous Qtz veins	pre to syn	Shear zone activation/lubrication by graphite accommodating pervasive fluid flow
Hoyle Pond deposit, Abitibi Greenstone Belt, Ontario, Canada	Dinel et al. (2008)	Graphite (via oxidation of organics)	Vein laminations; alteration zones in basaltic-komatiitic units; carbonaceous argillites	Auriferous Qtz veins	pre to syn	Devolatilization of CM-bearing rocks generated CO_2-rich fluid important for Au mobilization. Graphite results from oxidation of organic matter and/or via hydrothermal mineralization during fluid mixing; Au mineralization attributed to fluid mixing
Ashanti Gold Belt, Ghana	Oberthür et al. (1996); Berge (2011)	Graphite (via oxidation of organics)	Shear and fault zones in metaturbidites	Disseminated with sulfides; auriferous Qtz veins	pre to syn	Devolatilization of CM-bearing rocks generated CO_2-rich fluid important for Au mobilization. Graphite results from oxidation of organic matter and/or via hydrothermal mineralization

Table 1
Continued

| Deposit	Reference(s)	CM type	CM occurrence	Au occurrence	CM timing wrt. Au	Role of CM
Carbon Leader Reef, TauTona mine, Witswatersrand, South Africa	Parnell, (1996); Fuchs et al. (2017)	Pyrobitumen (via oxidation of oil)	Hydrocarbon seams in metasedimentary units	Dissemination is within wallrocks and pyrobitumen aggregates	pre (syn oxidation/ pyrolysis)	Reduction of aqueous auriferous fluid via mixing with uraniferous hydrocarbon fluid
Carlin deposits, Nevada, USA	Radtke and Scheiner (1970); Large et al. (2011)	Bitumen and pyrobitumen	Shales and calcareous mudstones	Refractory Au and inclusions in sulfides; disseminated free Au with organics	pre	Au liberated during Py recrystallization in carbonaceous shales resulting fom diagenesis and metamorphism. Carbonaceous units may act as source and sink.
Sukhoi Log deposit, Lena Gold Province, Russia	Razvozzhaeva et al. (2002); Large et al. (2007)	Pyrobitumen	Black shales	Dominantly refractory Au and inclusions in disseminated sulfides; Lesser Au in Py-Qtz veinlets	pre	Au-As initially concentrated in sulfide-rich carbonaceous black shales; later liberated during deformation/metamorphism.

Note. CM—carbonaceous material; Py—pyrite; Qtz—quartz; Urn—uraninite; wrt.—with respect to.
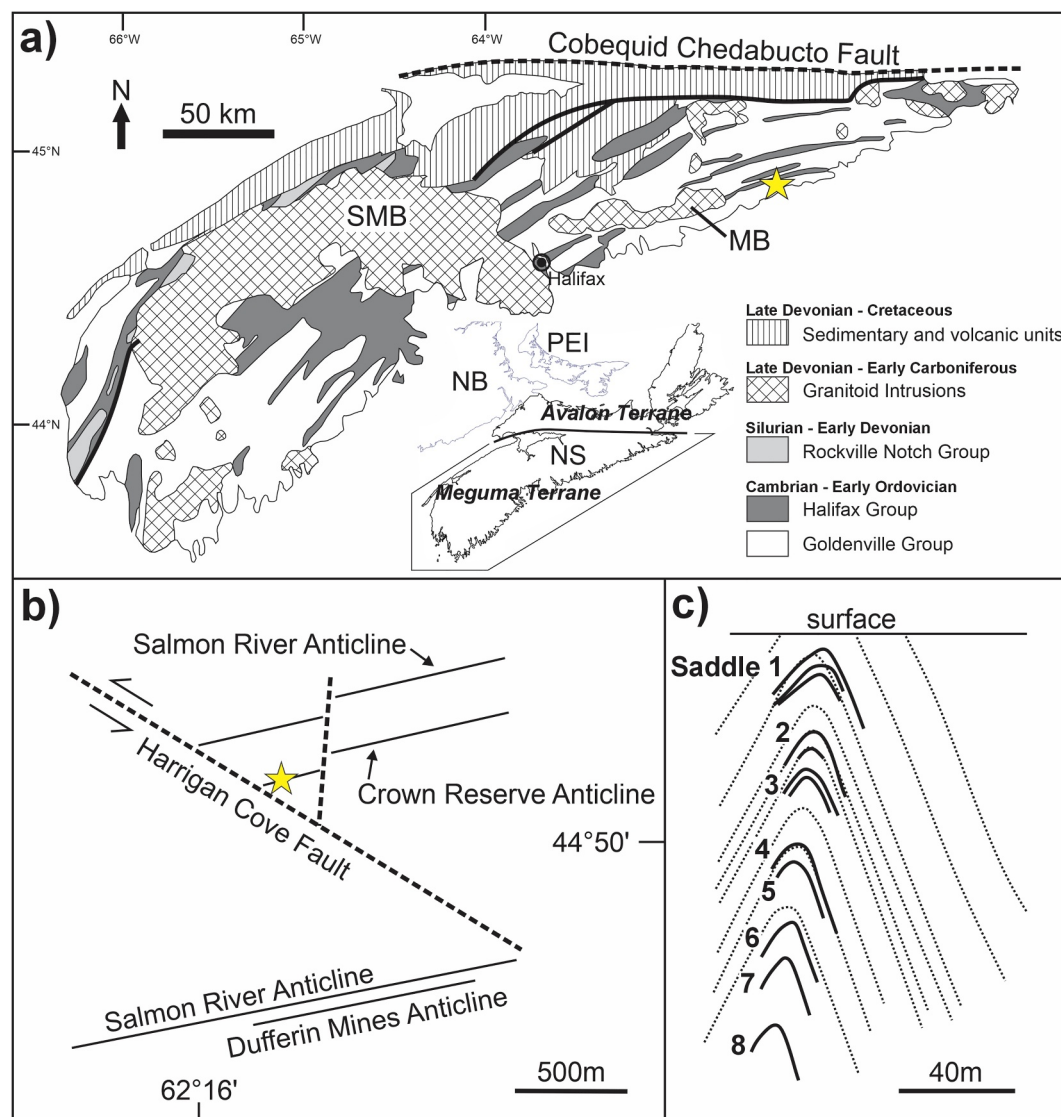
Figure 1. (a) Regional geological setting of the Meguma terrane of southern Nova Scotia. The location of the Dufferin deposit is shown (yellow star). SMB—South Mountain Batholith; MB—Musquodoboit Batholith. (b) Plan map of the Dufferin deposit with respect to local structural features. (c) Cross-sectional view of the Dufferin deposit (facing east) and fold structure showing the drill indicated geology with saddle veins highlighted by the thick black lines and bedding as dotted lines. Note that veins are localized to the lithological contacts of black fissile slate and metasandstone. Plan and cross-sectional maps modified after Horne and Jodrey (2001).

et al., 2012; Massonne et al., 2010). The Dufferin deposit lies ~20 km from the Musquodoboit Batholith and thus well outside its contact aureole (Figure 1a).

The Meguma terrane is well known for its numerous slate-belt-type gold deposits, which are characterized by massive to laminated, bedding-concordant quartz ± carbonate ± Fe sulfide veins (Kontak & Horne, 2010; Kontak et al., 1990; Malcolm, 1929; Ryan & Smith, 1998; Sangster & Smith, 2007). These deposits are mainly hosted throughout the metasandstone Goldenville Group, although some extend into the overlying slate-dominant Halifax Group; the deposits are preferentially localized to anticlinal hinges across the Meguma terrane (Horne & Culshaw, 2001; Kontak & Horne, 2010; Kontak et al., 1990; Sangster & Smith, 2007). Previous work indicates that these deposits generally conform to features of OGD with regard to vein types and fluid chemistry (Kontak & Horne, 2010). Importantly, both field relationships and direct dating ($^{40}Ar/^{39}Ar$, Re-Os) suggest that most deposits formed at ~380–370 Ma and thus overlap the emplacement of granitoid bodies across the Meguma
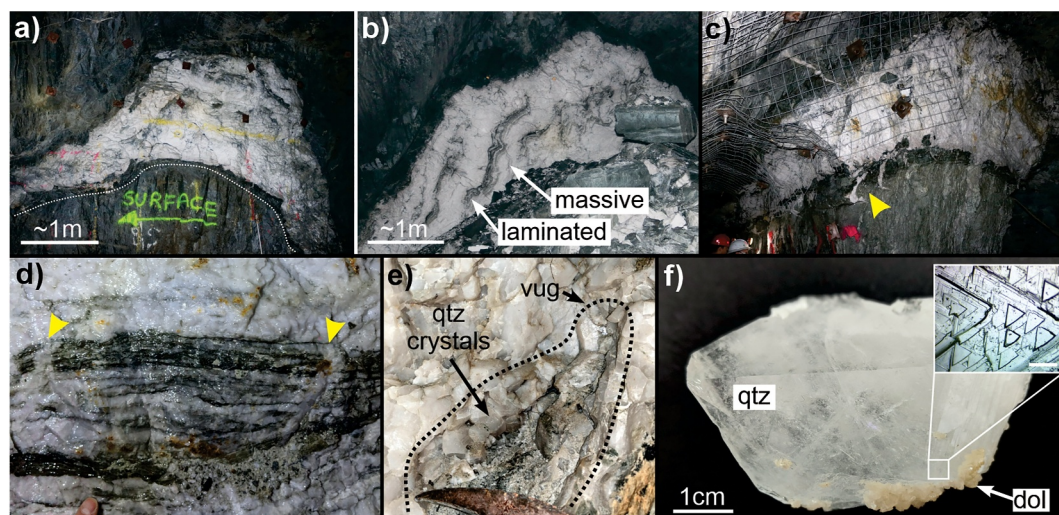
Figure 2. Saddle veins and vug-hosted quartz. (a) Underground exposure of saddles 3. Dotted white line outlines black slate. (b) Saddle 5 quartz vein showing both laminated and massive vein morphologies. (c) The dilated hinge zone of saddle 5 vein. Note the CM-bearing black slate and rotated en echelon veins (yellow arrow) along the saddle footwall. The limbs (legs) of this saddle have been extracted. (d) A segment of laminated vein surrounded by massive quartz. Note that extensions of the massive quartz veins crosscut earlier laminated veins (yellow arrows). (e) Translucent, euhedral quartz (qtz) crystals lining a cavity in the saddle 6 reef vein. These cavities frequently occur at the dilational zones of the saddle reef veins. Tip of rock hammer for scale. (f) A partially translucent euhedral quartz crystal extracted from a cavity. The surface of the quartz, which shows dissolution features (e.g., striate and triangular etch pits), is coated with euhedral dolomite (dol) ± pyrite. Scale bar in inset is ~1 mm.

terrane (see Kontak and Horne (2010) for review). This timing is consistent with the structural model of Horne and Culshaw (2001), where vein formation is related to late-stage fold tightening, as expected during batholith emplacement and related horizontal shortening (Benn et al., 1997).

The Dufferin deposit is hosted in a sandy flysch sequence of the Goldenville Group that is characterized by medium- to thickly bedded metasandstones with lesser metasiltstone and black slate comprising Bouma sequences (Harris & Schenk, 1975). Thus, a typical sedimentary cycle is characterized by graded metasandstone (~1 m) fining-upwards to metasiltstone (5–10 cm) and capped by black carbonaceous slate (1–5 cm; Horne & Jodrey, 2001); importantly, the auriferous bedding-concordant veins are localized to metasandstone-slate contact zones. The deposit is associated with a fault-bound portion of the Crown Reserve Anticline (Figure 1b) that consists of a tight plunging chevron fold which, from diamond drilling, is known to host at least 17 stacked saddle reefs with ≤700 m of strike continuity (Figure 1c; Hannon et al., 2017). Veining includes composite bedding-concordant saddle reefs (Figures 2a–2c) and their contiguous down-limb extensions (i.e., "leg" veins) with lesser discordant and en echelon vein types (yellow arrows in Figure 2c). All vein types are auriferous and can be related to flexural slip and hinge zone dilation (Hannon et al., 2017; Horne & Culshaw, 2001; Horne & Jodrey, 2001). The down-limb leg veins are commonly laminated (i.e., ribbon or crack-seal) and relate to incremental vein opening along bedding-parallel flexural slip movement horizons.

The hinge-hosted saddle-reef veins are composite and include both laminated and massive quartz vein generations (Figures 2b–2d) locally with quartz crystal-lined cavities/vugs (Figure 2e), which are the products of repeated intervals of dilation and fluid ingress. Carbonate (primarily ferroan dolomite) and sulfides (arsenopyrite, and more minor chalcopyrite, pyrite, galena, sphalerite) are common accessory phases in both vein and wallrock materials (Horne & Jodrey, 2001). Pyrite has been observed coating euhedral quartz crystals. Arsenopyrite specifically occurs as aggregates disseminated in the wallrock or in vein laminations (Horne et al., 2002). Gold occurs throughout the paragenesis within arsenopyrite as micro-inclusions and invisible Au (Gourcerol et al., 2020), and as visible gold within all vein types frequently spatially-associated with CM (see below). Importantly, gold commonly occurs along the margins of wallrock selvages (commonly along the footwall of saddle reef veins) and vein laminations, and as coarse-grained aggregates in saccharoidal massive quartz (cf., Horne & Jodrey, 2001; Hannon et al., 2017).

The deposit is low-tonnage with a current indicated resource of 151,500 tonnes yielding 58,000 oz of Au at 11.9 g/t, and an inferred resource of 703,000 tonnes yielding 150,000 oz of Au at 6.6 g/t (Hannon et al., 2017). Gold grade varies considerably among the saddle environments due to the nugget effect. Routinely assayed material within individual saddles may contain between 0.02 ("limit of detection" [LOD]) and >280 g/t Au. Assays of combined saddle and leg vein material from saddles 3 and 6, which are the focus of this study, average 4.6 ± 4.0 g/t and 12.4 ± 10.6 g/t, respectively (Hannon et al., 2017).

3. Methods

3.1. Sampling

Euhedral quartz crystals hosting abundant fluid inclusions were collected from vugs (Figures 2e and 2f) at dilational sites in saddle reef veins 3 and 6 near the apex of the anticline. Care was taken to select translucent quartz crystals that showed limited signs of recrystallization (e.g., milky white with saccharoidal texture). Quartz crystals cut sub-parallel to the c-axis were made into 200 μm thick fluid inclusion plates. Samples were also collected from a laminated down-limb leg vein from saddle vein 5 to investigate the mineralogy of carbonaceous vein laminations and associated gold occurrence.

3.2. SEM-EDS Analysis

Vein and vein lamination mineralogy, and elemental analysis/imaging of CM were investigated using a TESCAN MIRA 3 LMU VPS Field Emission Scanning Electron Microscope (SEM) at Saint Mary's University (Halifax, Canada) that is equipped with a back-scattered electron detector coupled with EDS functionality, and a Gatan miniCL imaging system that measures cathodoluminescent photons (185–850 nm). The instrument was operated at an accelerating voltage of 20 kV and an approximate working distance of 17 mm was used.

3.3. Fluid Inclusion Microthermometry

Fluid inclusion microthermometry was performed at Saint Mary's University using a Linkham FTIR600 heating-freezing stage mounted on an Olympus BX51 microscope. Temperature calibration was performed using synthetic fluid inclusion standards of pure H_2O (melting at 0°C and homogenization at the critical point of 374.1°C) and pure CO_2 (melting at −56.6°C; Tm_{CO2}). Uncertainties associated with microthermometric measurements range from ±2 to 3°C for temperatures recorded near the extremes of working conditions (i.e., −190 and 560°C) to ±0.1°C for temperatures near 0°C. For inclusion types containing a carbonic phase (L_{aq} + L_{car} + V_{car}; car = carbonic phase), salinity was determined based on the temperature of clathrate melting (Tm_{CLA}; Darling, 1991; Diamond, 1992). For inclusion types lacking observable clathrate nucleation, salinity was determined using the temperature of final ice melting (Tm_{ICE}; Bodnar & Vityk, 1994). The software packages BULK and ISOC (Bakker, 2003) were used to calculate bulk fluid inclusion compositions (informed from Raman spectroscopic analysis), molar volumes (cm³/mol) and isochores, utilizing temperatures and modes of total homogenization (Th_{TOT}), the homogenization of the CO_2 phase (Th_{car}) in carbonic phase-rich inclusions, and the estimated volumetric proportion of the carbonic phase at Th_{car}. Fluid inclusion microthermometric data can be found in Table S1.

3.4. Laser Raman Microspectroscopy (LRM)

Laser Raman microspectroscopy was performed at Saint Mary's University using a Horiba Jobin-Yvon LabRam HR confocal instrument equipped with a 100 mW (∼2 and 3 mW at sample surface through 100x Olympus MPLN objective) 532 nm Nd-YAG diode laser (Toptica Photonics) and Synapse charge-coupled device detector. Pure silicon was used as a frequency calibration standard. A 600 grooves/mm grating (spectral resolution of ca. ±2 cm^{-1}) was used for identification and mapping of fluid inclusion-hosted volatile species, whereas an 1800 grooves/mm grating (spectral resolution of ca. ±0.5 cm^{-1}) was used to accurately determine the Fermi diad spacing between the v_1 and v_2 Raman peaks of CO_2 (for ρCO_2 determination; Rosso & Bodnar, 1995). Semi-quantitative determination of the relative molar abundances of fluid inclusion-hosted volatile species followed the methodology of Beeskow et al. (2005, and references therein). Fluid inclusion Raman spectroscopic data can be found in Table S2.

3.5. Fluid Inclusion Laser Ablation Inductively Coupled Mass Spectrometry (LA-ICP-MS)

Fluid inclusion analysis by LA-ICP-MS was performed using a NWR 193 UC laser ablation system mounted to an Agilent 7900 quadrupole MS at the University of Toronto (Toronto, Canada). Gas flow rates of 1.0 L/min (He—carrier) and 0.85 L/min (Ar—make-up) were used, and tuning of the ICP-MS was done by monitoring mass-21/mass-42, ThO/Th, and U/Th ratios to achieve a ThO production rate of <0.3% and U/Th ~1. Dwell times were set to 10 ms, except for Au (100 ms), Ag (30 ms), As (20 ms), B (20 ms), S (40 ms), and Bi (20 ms). To avoid spalling, ablation was performed via stepwise expansion of the laser diameter to a final diameter ~5–10 μm larger than the inclusion being ablated. All analyte sensitivities, except for S, were calibrated using the reference standard SRM610 from NIST. Sulfur was calibrated using the Sca17 reference standard (Seo et al., 2011). Trace-element concentrations in bulk fluid inclusions were quantified using the software platform SILLS (Guillong et al., 2008), which involved deconvoluting the mixed inclusion + host signal from the host-only signal after calculation of background corrected count rates for each isotope. The salinity of the inclusions (wt.% equiv. NaCl), as determined by microthermometry, was used for internal standardization. Fluid inclusion LA-ICP-MS data can be found in Table S3.

3.6. C-Isotope Analysis of Carbonate

The carbon isotopic values ($\delta^{13}C$) for dolomite crystals coating the surface of a euhedral quartz crystal from saddle 6 were determined. Using a 0.4 mm tungsten carbide microdrill, approximately 30–60 μg of carbonate powder was removed from the dolomite. The carbon isotope ratios were measured using a Nu Perspective dual-inlet isotope ratio mass spectrometer connected to a NuCarb carbonate preparation system at McGill University Stable Isotope Laboratory (Montréal, Canada). Samples were calibrated to VPDB standard and data are reported in per mil (‰) with uncertainties of ±0.5‰ (1σ) as determined from analyses of standards.

4. Results

4.1. Vein Types, Mineralogy, Nature of CM and C Isotope Analysis

The saddle reef veins at Dufferin (Figures 2a–2d) consist of two distinct quartz variants: (a) early laminated quartz veins present in the hinges and the down-limb extensions of the saddles (i.e., saddle "legs"); and (b) volumetrically dominant massive quartz which incorporates fragments of, and crosscuts, earlier laminated veins. Of volumetrically lesser extent are discordant and en echelon (Figure 2d) vein quartz types, which are considered to be part of the saddle-forming vein event (Horne & Jodrey, 2001). In the laminated quartz veins, the wall rock-sourced septae comprise sericite + quartz + ferran dolomite + apatite + rutile + monazite ± arsenopyrite ± CM (Figure 3a). Locally, large vugs (~5–30 cm diameter) occur in massive quartz at, or proximal to, fold hinges and are lined with cm-sized euhedral quartz crystals (Figures 2c and 2d). The surfaces of quartz crystals are commonly coated with euhedral carbonate (ferran dolomite) ± pyrite and display dissolution features, including striate- and triangularly etched surface morphologies (Figure 2f). Two analyses of the ferran dolomite yielded $\delta^{13}C_{VPDB}$ values of −21.3 and −21.1‰.

In vein laminations and along vein margins, CM is locally abundant and occurs as amorphous, spheroidal, or blade-like masses coating cavities in fractures and between sericite cleavage planes (Figures 3b and 3c) and along quartz grain boundaries adjacent to septae margins (Figure 3d). The presence of C + S + Cl ± Na ± N in the CM was confirmed by SEM-EDS elemental maps, which show strong carbon enrichment compared to the associated dolomite (Figure 3f). However, these elements were unable to be quantified using this technique. Raman spectroscopy confirmed that the CM is not crystalline graphite but instead shares similar spectral characteristics (e.g., broad D and G spectral bands) to bitumen or pyrobitumen (Figure 3g; Jehlicka et al., 2003; Kouketsu et al., 2014; Liu et al., 2013). The Raman geothermometer of Kouketsu et al. (2014) evaluates the morphology of spectral features (e.g., D and G spectral bands in the region of ~1,000–1,800 cm^{-1}) as a function of CM maturity, which indicates that the CM was subjected to a maximum temperature of 300 ± 30°C. Intimately associated with the CM are arsenopyrite and native gold (88–92 at. % Au; Ag balance). Arsenopyrite with a euhedral habit is observed in fractures with abundant CM, with CM adjacent to and coating arsenopyrite grains (Figure 3d). Carbonaceous material and gold are observed together lining interstitial spaces along grain boundaries (Figures 3e and 3f; red arrows) in addition to micron-scale native gold grains (<2 and 3 μm) that occur embedded in CM (Figure 3e; yellow arrows in inset). Micron-scale grains of quartz, rutile and pyrite are also common in the CM.
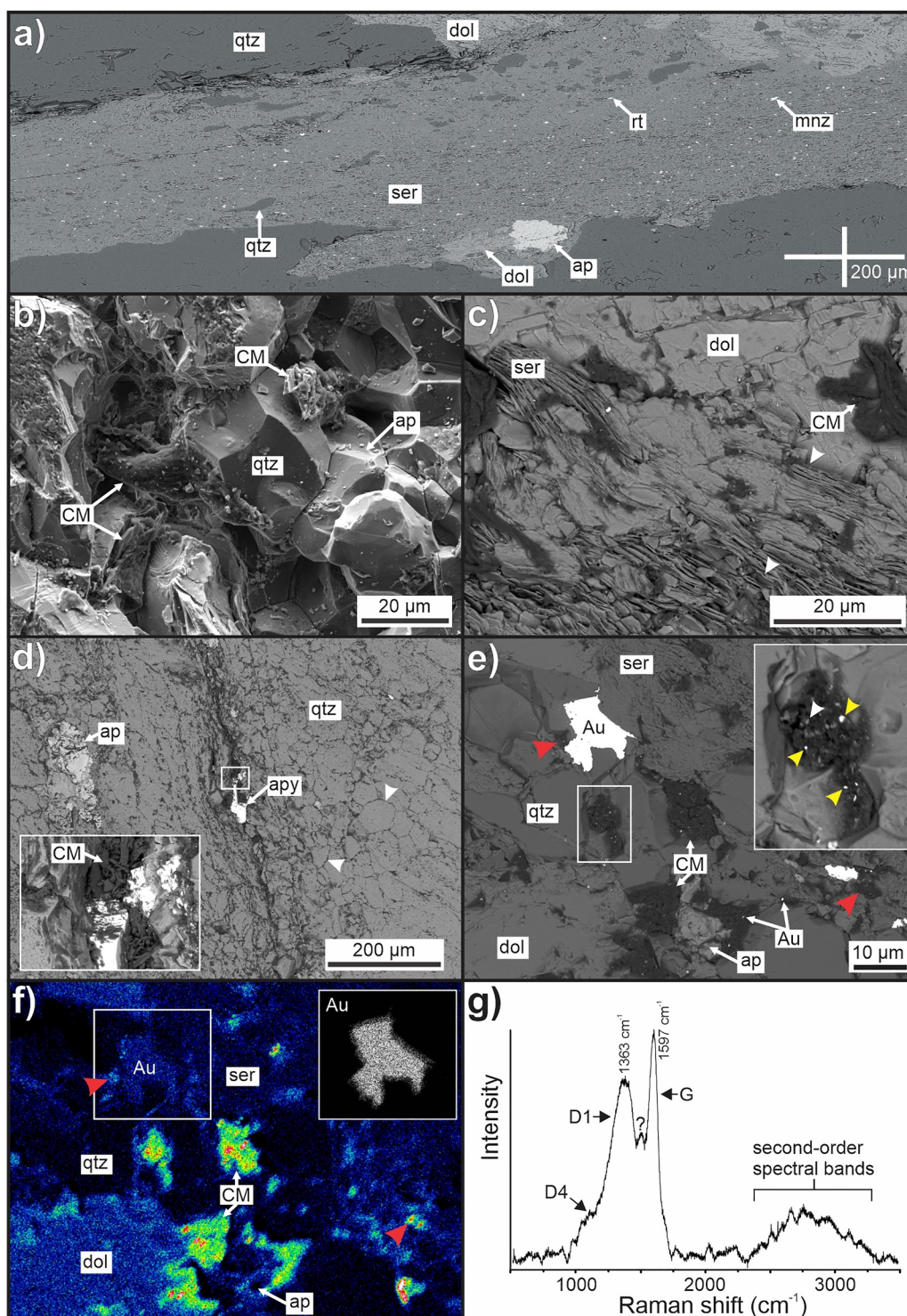
Figure 3.

4.2. Fluid Inclusion Systematics

4.2.1. Fluid Inclusion Petrography and Microthermometry

In the euhedral quartz crystals from cavities in saddles 3 and 6, three distinct fluid inclusion types are recognized based on petrographic, microthermometric, and Raman spectroscopic characteristics. Relationships between these fluids, CM, and gold are discussed in subsequent sections, and their petrographic and compositional features are summarized in Table 2 and the complete microthermometric data set is listed in Table S1.

Fluid inclusions are classified in the context of fluid inclusion assemblages (FIA) by establishing the relative timing of entrapment for groups of texturally coeval inclusions (cf., Goldstein & Reynolds, 1994; Bodnar, 2003). Fluid inclusion types are mainly distinguished by differences in composition and phases identified through observations at 20°C supplemented with thermometric measurements and Raman analysis, as noted below.

Type 1 inclusions contain an aqueous-carbonic fluid and show some variation based on morphology, composition and phase proportion. *Type 1a* inclusions ($n = 36$; Figure 4a), commonly having negative crystal shapes, are three-phase ($L_{aq} + L_{car} + V_{car}$; car = carbonic phase) at 20°C, with an aqueous phase proportion of 63 ± 5 vol.% (determined petrographically via image analysis). These inclusions show carbonic phase melting (Tm_{car}) and carbonic phase homogenization (Th_{car}) at -57.2 ± 0.4°C and 25.9 ± 1.4°C, respectively. The mode of Th_{car} varies between liquid and vapor, and likely reflects variable ρCO_2 and/or CH_4 and N_2 abundances in the carbonic phase. Type 1a inclusions have aqueous phase and bulk fluid salinity of 1.3 ± 0.4 and 0.9 ± 0.3 wt.% NaCl equiv., respectively, based on clathrate melting (Tm_{CLA}) values between 9.1 and 10°C (cf., Darling, 1991; Diamond, 1992). Type 1a inclusions have a temperature of total homogenization (Th_{TOT}) to liquid at 287 ± 8°C. Note that the carbonic phase contains variable concentrations of CO_2, CH_4, N_2, H_2S and hydrocarbons as described in the next section.

Type 1b inclusions ($n = 52$; Figure 4b) are two-phase ($L_{aq} + V_{car}$) at 20°C. Due to the lower abundance of CO_2 in these inclusions, a thin film of L_{car} may surround the vapor phase but is optically obscured by the high relief of the inclusion margin; therefore, Tm_{car} and Th_{car} could not be accurately measured. These inclusions have an aqueous phase proportion of 79 ± 5 vol.%, and aqueous phase and bulk fluid salinity of 4.6 ± 0.5 and 4.1 ± 0.5 wt.% NaCl equivalent, respectively, based on the temperature of final ice melting (Tm_{ICE}). Type 1b inclusions show a Th_{TOT} to liquid at 241 ± 21°C. As clathrate melting was not observed, the reported salinity values may modestly overestimate aqueous phase salinity.

Type 2 fluid inclusions ($n = 37$; Figure 4c) appear petrographically similar to type 1b inclusions, that is, they are also two-phase ($L_{aq} + V_{car}$) at 20°C and have an aqueous phase proportion of 86 ± 3 vol.%. These inclusions often show a higher aqueous phase volume percentage than type 1b inclusions but are differentiated based on their microthermometric and Raman spectroscopic properties and bulk compositions (Table 2). They have aqueous phase and bulk fluid salinity of 3.2 ± 1.0 and 3.0 ± 0.9 wt.% NaCl equivalents, respectively, and show Th_{TOT} to liquid at 210 ± 9°C.

No evidence of a primary origin for any of the fluid inclusions (i.e., trapped along growth zones) was observed during the petrographic study and is confirmed by cathodoluminescence (CL) imaging of several euhedral quartz crystals. The CL imaging shows that *all* the fluid inclusion types are confined to planes and irregular patches of secondary quartz that crosscut primary growth zones and display weaker (darker) luminescence intensity than in regions absent of fluid inclusions (Figure 4d). Where trails of type 1a FIA are crosscut by type 2 FIA, some type 1a inclusions appear to have been emptied, refilled by later type 2 fluid, and resealed (Figure 4e; e.g., Goldstein, 1986; Touret, 1981).

Figure 3. Microscopic and Raman spectroscopic features of Au-mineralized septa in vein laminations. (a) Wallrock septa in laminated quartz vein dominated by sericite + quartz + ferroan dolomite + apatite with subordinate monazite + rutile ± Au. (b) A secondary electron image showing carbonaceous material (CM) in a vein lamination. (c) A back-scattered electron (BSE) SEM image of CM in interstitial spaces between grain boundaries, fracture in dolomite, and between cleavage planes of sericite (white arrows). (d) A BSE-SEM image of CM in an arsenopyrite-bearing fracture and along quartz grain boundaries (white arrows). (e) A BSE-SEM image showing gold in an exposed quartz-sericite-dolomite-apatite lamination in saddle 5 leg vein. Note that CM and gold cooccupy the same structures (red arrows) and that CM hosts abundant submicron gold grains (yellow arrows in inset) and pyrite (white arrow in inset). (f) A SEM-EDS map of the field of view in frame (e) showing elemental carbon relative abundance (in color temperature scale). Note that carbon in the CM-filled cavities is highly enriched relative to dolomite. (g) A representative Raman spectrum of the CM (with D, G, and second-order Raman bands shown; cf., Jehlicka et al., 2003; Kouketsu et al., 2014) that is associated with submicron diameter gold grains in frame (c). Abbreviations: ap—apatite; apy—arsenopyrite; CM—carbonaceous material; dol—dolomite; qtz—quartz; ser—sericite.

Table 2
Fluid Inclusion Types Identified in the Dufferin Quartz Veins and Corresponding Compositional Data

|	FI types		
Properties	Type 1a ($L_{aq} + L_{car} + V_{car}$)	Type 1b ($L_{aq} + V_{car}$)	Type 2 ($L_{aq} + V_{car}$)
Phases present at 21°C	$(H_2O\text{-}NaCl)_L + (CO_2)_L + (CO_2 \pm CH_4 \pm N_2)_V$	$(H_2O\text{-}NaCl)_L + (CO_2 \pm CH_4 \pm N_2)_V$	$(H_2O\text{-}NaCl)_L + (CO_2 \pm CH_4 \pm N_2)_V$
Total # of inclusions measured	41 (9 FIA)	52 (9 FIA)	37 (6 FIA)
FI size (μm)	≤150	≤150	≤250
vol.% aqueous liquid phase at 21°C	53–79 (63 ± 5); $n = 36$	69–89 (79 ± 5)	75–93 (86 ± 3)
Tm_{ICE}	ND	−2.4 to −3.4; $n = 52$	−1.0 to −2.9; $n = 37$
Tm_{CLA}	9.1–10; $n = 36$	ND	ND
Aq. phase salinity (wt. % NaCl equiv.)	0.1–1.9 (1.3 ± 0.4); $n = 36$	4.0–5.6 (4.6 ± 0.6); $n = 52$	1.7–4.7 (3.2 ± 1.0); $n = 37$
Bulk salinit (wt. % NaCl equiv.)	0.1–1.4 (0.9 ± 0.3); $n = 36$	3.5–5.1 (4.1 ± 0.5); $n = 52$	1.6–4.4 (3.0 ± 0.9); $n = 37$
Tm_{CO2}	−58.4 to −56.4 (−57.2 ± 0.6); $n = 33$	ND	ND
Th_{CO2}	19.8–27 (25.9 ± 1.4); $n = 32$	ND	ND
Th_{TOT}	269–310 (286 ± 8); $n = 30$	221–302 (241 ± 21); $n = 40$	190–235 (210 ± 9); $n = 34$
BULK			
ρ_{BULK} (g/cm^3)	0.76–0.94 (0.89 ± 0.04); $n = 36$	0.82–0.97 (0.90 ± 0.04); $n = 52$	0.79–0.96 (0.90 ± 0.03); $n = 37$
X_{NaCl}	0.007 ± 0.0026; $n = 33$	0.027 ± 0.0034; $n = 52$	0.019 ± 0.0066; $n = 37$
X_{CO2}	0.151 ± 0.028; $n = 33$	0.05 ± 0.009; $n = 52$	0.022 ± 0.005; $n = 37$
X_{CH4}	0.002 ± 0.001; $n = 33$	0.0003 ± 0.0002; $n = 52$	0.0007 ± 0.0002; $n = 37$
X_{N2}	0.009 ± 0.002; $n = 33$	0.002 ± 0.0001; $n = 52$	0.003 ± 0.001; $n = 37$
VAPOR PHASE			
ρ_{CO2} (g/cm^3)	0.4 ± 0.2; $n = 17$	0.23 ± 0.1; $n = 18$	0.1 ± 0.05; $n = 16$
X_{CO2}	0.951 ± 0.014; $n = 22$	0.915 ± 0.031; $n = 20$	0.598 ± 0.07; $n = 16$
X_{CH4}	0.006 ± 0.007; $n = 22$	0.013 ± 0.009; $n = 20$	0.073 ± 0.023; $n = 16$
X_{N2}	0.042 ± 0.01; $n = 22$	0.072 ± 0.025; $n = 20$	0.328 ± 0.051; $n = 16$
X_{H2S}	–	–	–

Note. Fluid inclusion size represent the approximate maximum cross-sectional dimension observed. All temperature data reported in °C. Tm_{CO2} temperatures >-56.6°C reflect cumulative measurement uncertainty. Salinity of the aqueous phase was determined via final ice melting temperature or clathrate melting temperature. X_{NaCl}, X_{CO2}, X_{CH4}, X_{N2}, and X_{H2S} represent bulk fluid inclusion values calculated using the program BULK (Bakker, 2003) or vapor phase compositions determined by Raman spectroscopic analysis. Bulk density values were calculated by applying the equations of state outlined by Bowers and Helgeson (1983) and Bakker (1999). CO_2 density was determined using the Fermi diad spacing between spectral peaks (after Rosso & Bodnar, 1995). Errors (including data in brackets) represent ±1σ standard deviation. aq.—aqueous; car—carbonic; FIA—fluid inclusion assemblage; ND—not determined/not observed; Tm_{ICE}—final ice melting; Tm_{CLA}—final clathrate dissociation; Tm_{CO2}—final melting of CO_2; Th_{CO2}—CO_2 homogenization; Th_{TOT}—total homogenization temperatures.

4.2.2. Fluid Inclusion Laser Raman Microspectroscopy

Analyses of fluid inclusion vapor phases by LRM show that whereas the bulk compositions of types 1a and 1b inclusions are different, their volatile contents are similar (Figure 5a; Table S2). An LRM map of a large (∼100 μm diameter) type 1a fluid inclusion (Figures 5b–5i) reveals significant features of the fluid chemistry of these Au-bearing (see Section 4.2.3 for Au concentrations) aqueous-carbonic fluids. In contrast, type 2 fluid inclusion vapor phases are characteristically richer in CH_4 and N_2 (i.e., by about an order of magnitude) relative to types 1a and 1b fluid inclusions (Figures 5a and 5j), and consequently have lower vapor phase $CO_2/(CH_4 + N_2)$ ratios (18 ± 1, 11 ± 1, and 1.3 ± 1 for type 1a, 1b, and 2 inclusions, respectively; Table S2). Analyses of the aqueous phases show that both type 1a and 1b inclusions contain B as boric acid, which was not detected in type 2 inclusions (Figures 5d and 5k). All fluid inclusion types contain the aqueous carbonic species $CO_{2(aq)}$ and $HCO_3^-{}_{(aq)}$. The main Raman shift for $CO_3^{2-}{}_{(aq)}$ (∼1,064 cm^{-1}) overlaps with a quartz host shift at ∼1,066 cm^{-1} of variable intensity depending on crystallographic orientation (Frezzotti et al., 2012), thus $CO_3^{2-}{}_{(aq)}$ could not be accurately identified. Although only qualitative, type 2 inclusions show a more intense signal for $HCO_3^-{}_{(aq)}$ relative to $CO_{2(aq)}$ compared to type 1a and type 1b inclusions under the same analytical parameters (Figure 5k).
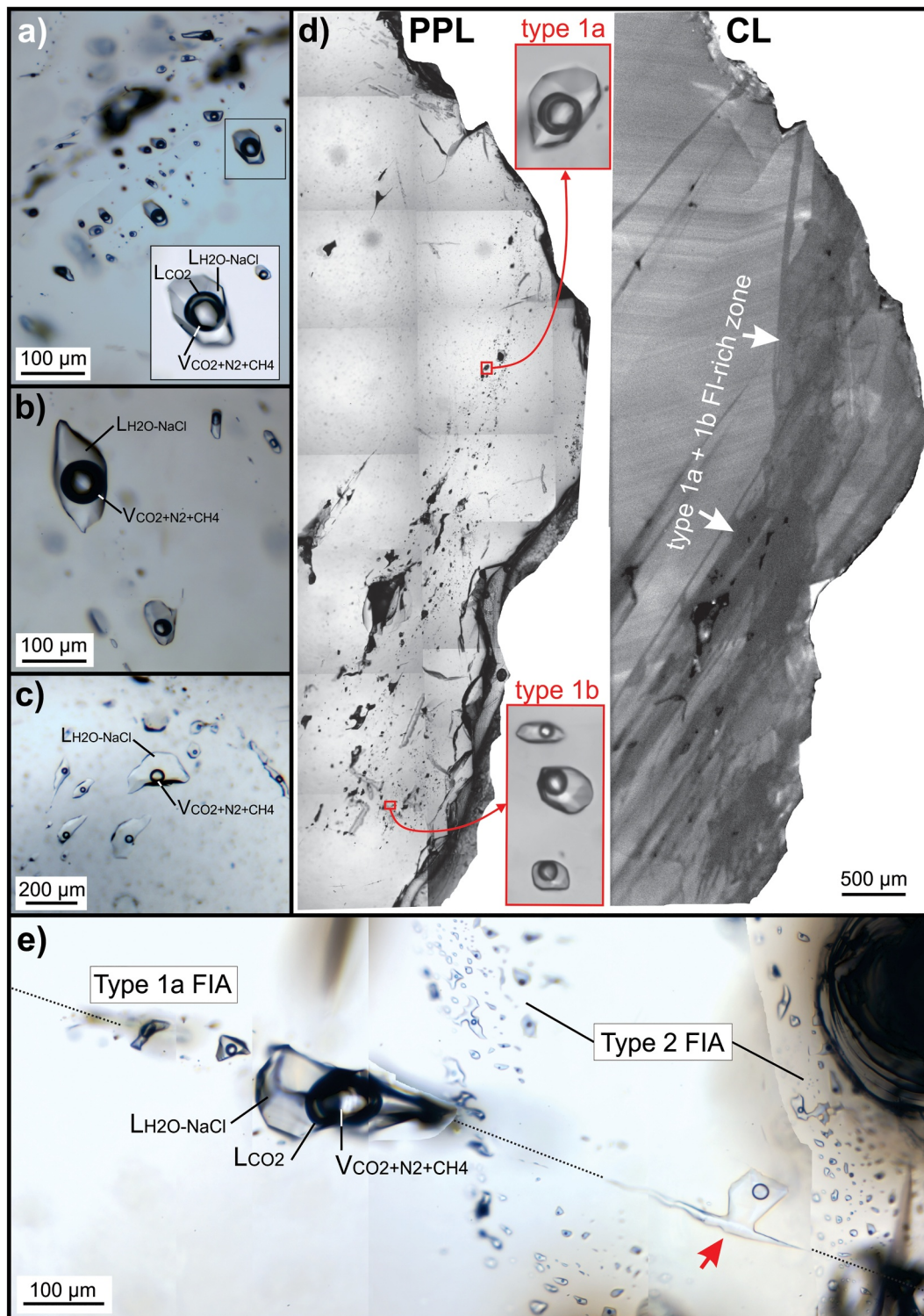
Figure 4. Petrographic characteristics of quartz-hosted fluid inclusions from veins in saddles 3 and 6. (a) A fluid inclusion assemblage (FIA) of secondary type 1a, three-phase, H_2O-NaCl-CO_2 ($+N_2 + CH_4$) inclusions. (b) A FIA of secondary type 1b, two-phase H_2O-NaCl + CO_2 ($+N_2 + CH_4$) inclusions. (c) A FIA of secondary type 2, two-phase H_2O-NaCl + CO_2 ($+N_2 + CH_4$) inclusions displaying a low vapor to liquid ratio. (d) A transmitted plane polarized light (PPL) photomicrograph (left) with a corresponding enhanced-contrast SEM cathodoluminescence (CL) image (right) of a region within a vug-hosted euhedral quartz crystal. No primary fluid inclusions associated with quartz growth zones are observed rather all fluid inclusion assemblages (e.g., type 1a and 1b inclusions shown in insets) are hosted in secondary quartz with low CL intensity (white arrows) that crosscut primary zoning. Fluid inclusion-rich secondary quartz is associated with healed fractures/planes or irregular patches. (e) Trail of type 1a FIA crosscut by type 2 FIA. A type 1a inclusion has been emptied and refilled with type 2 fluid (red arrow).
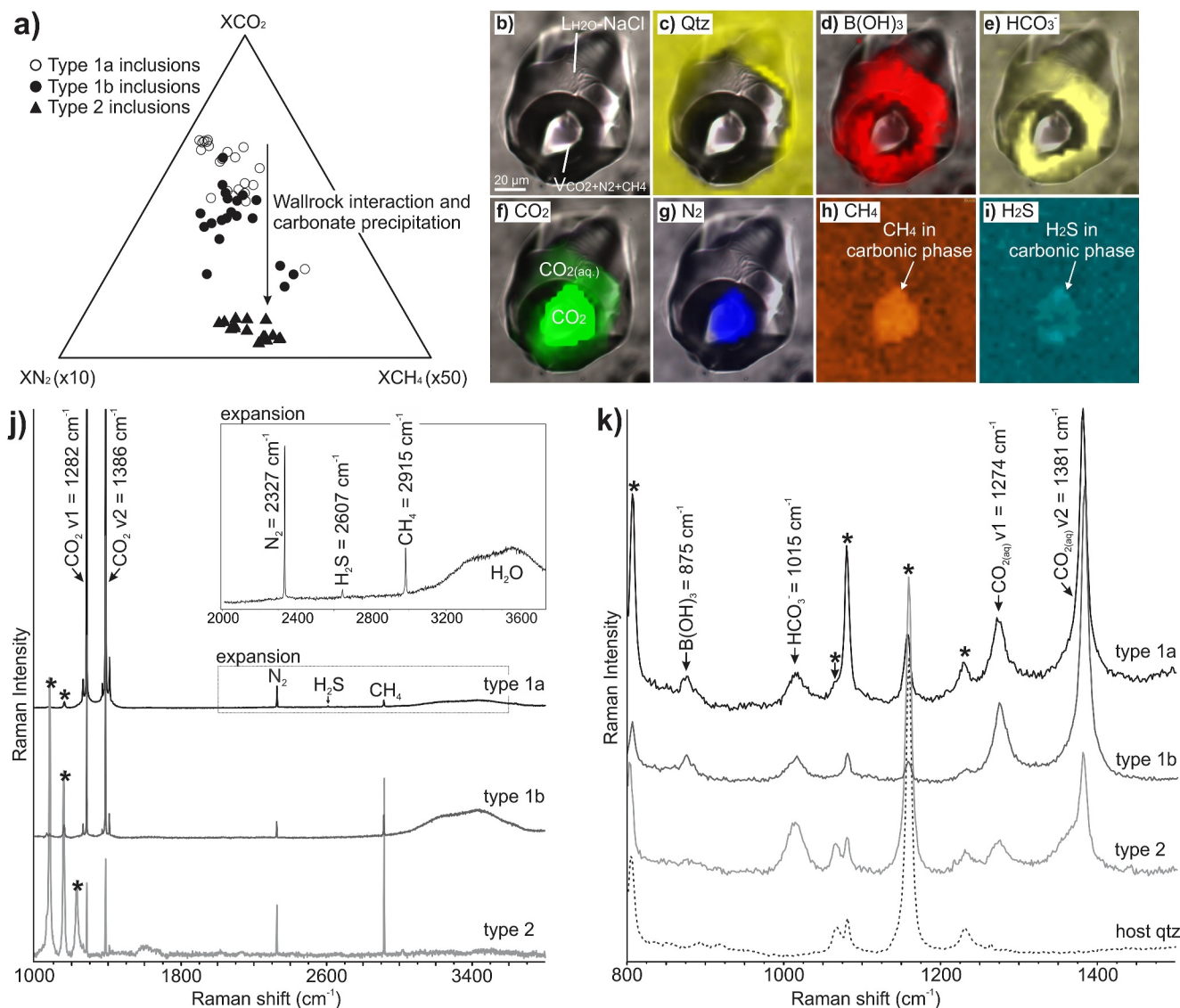
Figure 5. Raman spectra and molecular maps. (a) Raman quantification of CO_2, CH_4 and N_2 in fluid inclusion vapor phases (from saddles 3 and 6). Note that types 1a and 1b inclusions display similar vapor phase gas contents despite differences in their bulk compositions, whereas type 2 inclusions display enrichment in N_2 and CH_4 relative to type 1a and 1b inclusions. (b) A Type 1a fluid inclusion mapped via laser Raman microspectroscopy. The carbonic phase (i.e., L_{CO_2} + V_{CO_2}) was homogenous during mapping. (c) Quartz host map. (d) Boric acid map. Boric acid was only detected in the aqueous phase. (e) HCO_3^- (bicarbonate) map. Bicarbonate was only detected in the aqueous phase. (f) CO_2 map showing $CO_{2(aq)}$ and CO_2 in the carbonic phase. (g) N_2 map. N_2 was detected only in the carbonic phase. (h) CH_4 map. CH_4 was detected only in the carbonic phase. The fluid inclusion is excluded for clarity. (i) H_2S map. Only very trace H_2S was detected in the carbonic phase. The fluid inclusion was excluded for clarity. (j) Raman spectra of the vapor phases of types 1a, 1b, and 2 fluid inclusions. Raman spectrum of quartz host is shown for reference. (k) Raman spectra of the aqueous phases of types 1a, 1b, and 2 fluid inclusions. Note: Raman shifts of the quartz host are indicated with asterisks.

The average densities of CO_2 in type 1a, 1b, and 2 fluid inclusion vapor phases, determined based on the Fermi diad spacing between v_1 and v_2 CO_2 Raman shifts (cf., Rosso & Bodnar, 1995), were 0.4 ± 0.2, 0.23 ± 0.1, and 0.1 ± 0.05 g/cm³, respectively. Despite the compositional and density differences among the fluid inclusion vapor phases, types 1a, 1b, and 2 inclusions have identical bulk densities (0.89 ± 0.04, 0.9 ± 0.04, and 0.9 ± 0.03 g/cm³, respectively; see Table 2); thus, all isochore ranges overlap in P-T space (Figure 6).

4.2.3. Fluid Inclusion LA-ICP-MS

The results of LA-ICP-MS analysis of type 1a (n = 84) and type 2 fluid inclusions (n = 32) are presented in Figure 7a and Table S3. Type 1b inclusions were not analyzed due to optical limitations during analysis, as the refractive nature of the large carbonic phase bubbles made it difficult to discern whether the inclusion was a type
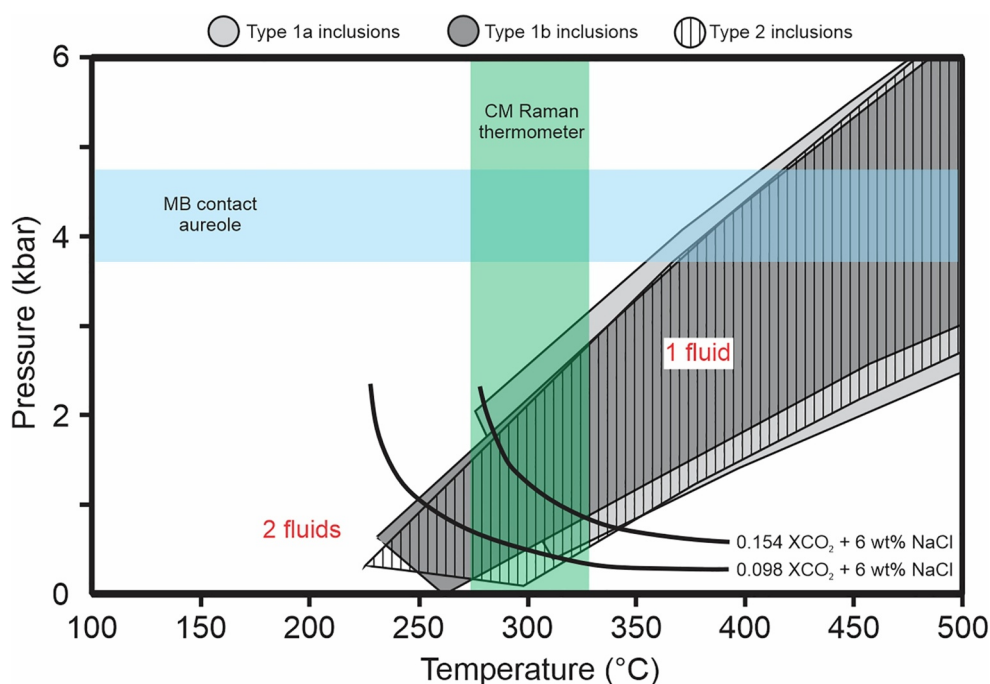
Figure 6. Isochoric fields for all inclusion types. Note that all fluid inclusion types display nearly identical bulk densities and thus their isochores overlap in PT space. Lines representing approximate maxima solvi (i.e., as the measured salinity in this study are all ≤5 wt. % NaCl) are shown that separate 2-phase (i.e., unmixed aqueous-carbonic fluids) from 1-phase (i.e., homogeneous fluid) fields for two distinct fluid compositions (Gehrig, 1980). The green field represents the inferred temperature to which CM-bearing vein septa/lamellae were subjected based on Raman spectral characteristics of CM (cf., Kouketsu et al., 2014). The blue field represents the inferred pressure conditions of the contact aureole associated with the Musquodoboit Batholith (MB) based on syn-magmatic muscovite crystallization (Kontak & Kyser, 2011; Massonne et al., 2010). Note how the addition of volatiles (e.g., CH_4, N_2), and/or solute species (e.g., NaCl) increases the P-T range of immiscibility.

1a or 1b; therefore, only inclusions with optically obvious double bubbles ($L_{CO2} + V_{CO2}$) were targeted as type 1a inclusions. Figure 7b shows a representative LA-ICP-MS transient signal from the ablation of a type 1a inclusion with corresponding calculated element concentrations shown in Figure 7b. The LOD values are noted to be inclusion-specific, and element concentrations below routine LOD are excluded from calculated averages and standard deviations. Elemental concentrations show no relationship to fluid inclusion size.

Among FIA of the same fluid inclusion types (e.g., various type 1a FIA), elemental concentrations can vary substantially within the same order of magnitude, resulting in significant 1σ standard deviations. Therefore, elemental concentrations among fluid inclusion populations are reported as the interquartile ranges (i.e., data between Q1 and Q3) where appropriate. Importantly, we note that for individual FIA the metal contents, such as As, Sb, and Au, can be very consistent. For example, in a single type 1a FIA (see Table S3; Figure S1 in Supporting Information S1) constituting eight fluid inclusions, Au concentration varied between 36.7 and 63.5 ppb (average of 55.4 ± 9.7 ppb; 1σ).

Concentrations of B between type 1a (260–420 ppm) and type 2 (195–415 ppm), and S between type 1a (150–400 ppm) and type 2 (140–270 ppm) fluids are similar. With regard to S, in both fluid inclusion populations it was often below routine LOD such that only 19% of type 1a inclusions and 13% of type 2 inclusions contained concentrations above the LOD. Notably, the average concentrations of As and Sb were significantly higher in type 1a inclusions (30–85 ppm and 16–40 ppm, respectively) than in type 2 inclusions (2–15 ppm and 2–8 ppm, respectively). Gold was detected in 70% of analyzed type 1a inclusions, averaging 44.7 ± 24.5 ppb (1σ) for values above the LOD. Conversely, Au was detected in 22% of analyzed type 2 inclusions, averaging 24.7 ± 12.3 ppb (1σ). A positive correlation between fluid concentrations of Au and As (Figure 7c), and Au and Sb (Figure 7d) is present.

Type 2 fluids are relatively enriched in Mg (300–1245 ppm) and Ca (1,485–3,205 ppm) compared with type 1a fluid inclusions (40–230 ppm and 490–1,350 ppm, respectively). Type 2 fluids are also relatively enriched in Sr
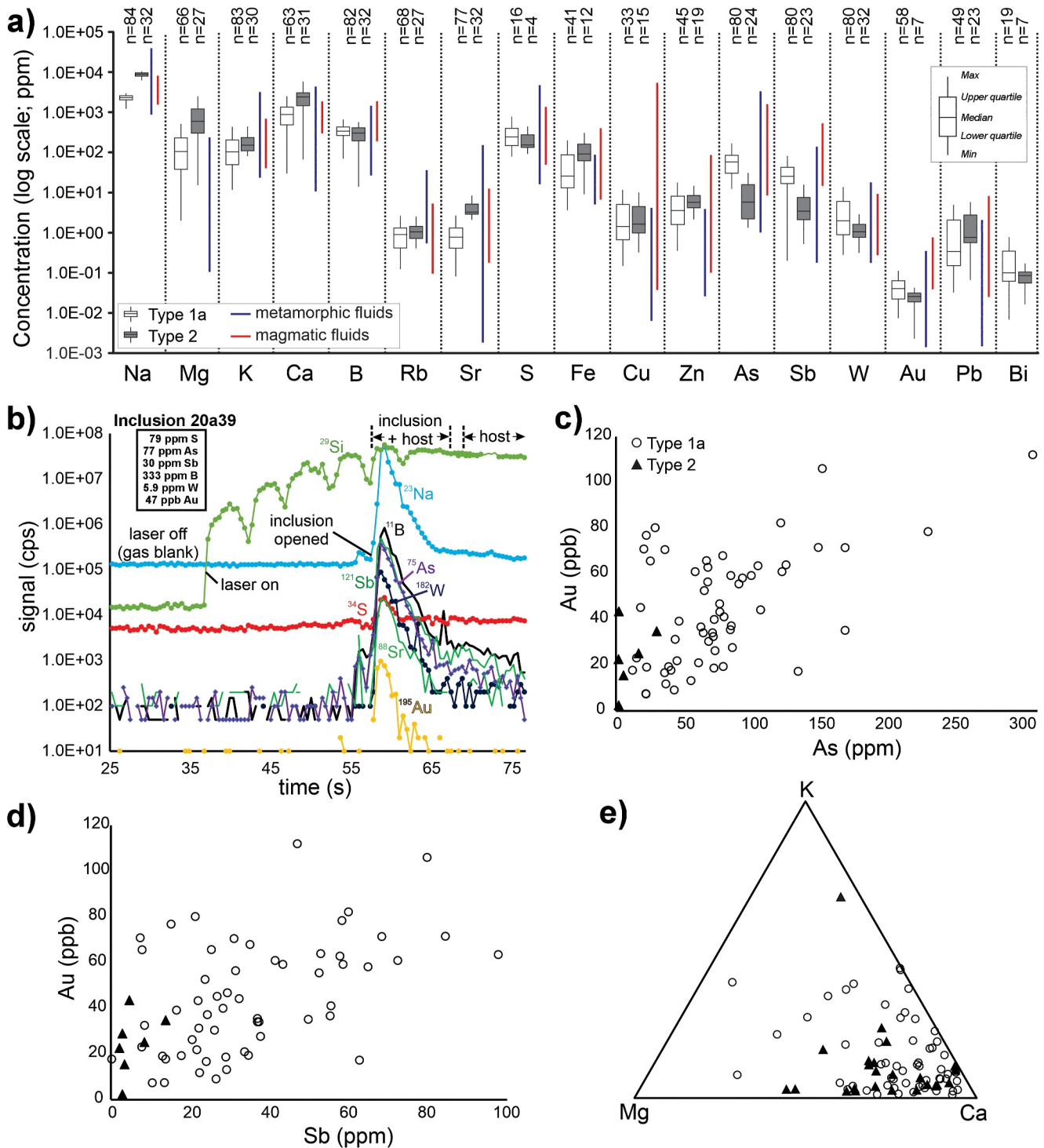
Figure 7. LA-ICP-MS quantified elemental concentrations and signal. (a) LA-ICP-MS data for type 1a ($n = 84$) and type 2 ($n = 32$) fluid inclusions. Note that element concentrations below analytical limits of detection, which are element specific, are excluded from statistical treatment; thus, the number of analyses is different depending on which fluid inclusion type and element is considered (i.e., see "n" values at top of plot). Ranges for unmixed metamorphic fluids (Fusswinkel et al., 2017; Marsala et al., 2013; Miron et al., 2013; Rauchenstein-Martinek et al., 2014) and magmatic fluids (Williams-Jones & Heinrich, 2005 and references therein) are shown for comparison. The ends of the whiskers are set to $1.5 \times$ IQR (interquartile range) above and below the third and first quartiles, respectively. Outliers are not plotted for clarity. (b) LA-ICP-MS signal (count rate vs. time) from a type 1a inclusion. The complete LA-ICP-MS data set for all analyzed inclusions can be found in Table S3. (c, d) As versus Au ($R^2 = 0.746$), and Sb versus Au ($R^2 = 0.752$) biplots of fluid inclusion LA-ICP-MS compositional data. Only data points above LOD have been plotted. (e) Mg-K-Ca ternary for type 1a and type 2 fluid inclusions showing overlapping fluid compositions with minor enrichment of K in type 1a relative to type 2 inclusions.

(3–5 ppm) and Fe (60–160 ppm) compared with type 1a fluids (0.5–1.5 ppm and 15–90 ppm, respectively). Potassium concentrations are similar in both type 1a (50–200 ppm) and type 2 (110–240 ppm) inclusions.

The higher absolute concentrations of aqueous chloride-complexed cations (i.e., Mg, K, Ca, Rb, Sr, Fe, Cu, Zn, and Pb) in type 2 inclusions are a result of the bulk salinity difference among inclusion types, as relative concentrations of these species in type 1a and 2 fluids are similar (e.g., Mg-K-Ca ternary; Figure 7e).

5. Discussion

5.1. Vein Paragenesis and the Timing of Gold-Enriched Fluids

A protracted history of hydrothermal and deformational activity at the Dufferin deposit is indicated at the deposit scale by the presence of early laminated bedding-concordant vein types that are in turn overprinted by later massive veins coeval with flexural slip-related fold hinge dilation, saddle reef development, and likely migration of early laminated veins to hinge areas (Horne & Jodrey, 2001; Horne & Culshaw, 2001; Figure 2b). Flexural slip and fold hinge dilation was repeated in each of the numerous multiply stacked saddle reef veins, but the sequence of saddle formation is not known. This history is reflected in the petrography of fluid inclusions whereby CL imaging of euhedral quartz crystals from vugs shows zoned primary quartz completely devoid of fluid inclusions with discordant lower CL-luminescent secondary quartz zones occupying healed fractures and other planar features, and irregular patches. These secondary quartz domains, originating from coupled dissolution precipitation (CDP) of the original vein quartz material, host abundant FIA that were trapped at the time of generation of these secondary quartz domains and are thus primary with respect to the new quartz (type 1a, 1b, and 2 inclusions; Figure 4d) but of secondary origin relative to the earlier zoned quartz. A similar origin for the generation of low-luminescent quartz domains via CDP processes is well established based on several studies of porphyry deposit settings (e.g., Mao et al., 2017; Monecke et al., 2018; Rusk, Reed, Bignall, & Tsuchiya, 2004). Thus, while fluids trapped in vug-hosted quartz from the hinge zones of saddle veins (Figure 2) are broadly synchronous with the overall vein sequence, they are *late* relative to the formation of the host saddle but may generally be *early, coeval, or late* relative to other saddles in the stacked sequence. Importantly, the Dufferin aqueous-carbonic inclusions (type 1a, b) within secondary domains of low-luminescent quartz have compositions consistent with inferred ore fluids reported in Meguma-hosted deposits (Bierlein & Smith, 2003; Kerr et al., 2021; Kontak et al., 1990, 1996) and other OGD settings (see above references).

The secondary origin of Au- and S-bearing fluid inclusions, and absence of any primary fluid inclusions in the quartz veins, is consistent with the late paragenesis for some of the gold at Dufferin, as indicated by numerous textural associations including gold located at quartz grain boundaries, in cavities and along septa margins, and an abundance of coarse-grained aggregate gold within massive, non-laminated quartz (Hannon et al., 2017). As noted herein, the intimate association of micron-scale gold with CM represents another gold occurrence at Dufferin that is also a well-documented feature at other gold settings, including OGD (Table 1). Importantly, the CM-Au relationship is paragenetically late in the evolution of vein formation. Together with other textural variants of Au, this indicates an overall protracted paragenesis for Au at Dufferin and does not preclude remobilization of said gold from earlier occurrences (e.g., Gourcerol et al., 2020; Hastie et al., 2020 and references therein).

5.2. Auriferous Fluid Composition and P-T-X Evolution at Dufferin

In OGD, the relationship between episodes of initial Au deposition and changes in specific physicochemical parameters in aqueous-carbonic fluids with time (e.g., fluid gold content, pH, volatile chemistry) may only be resolved through comprehensive fluid inclusion studies integrated with petrography; however, these are rarely investigated and only a few studies globally have measured Au contents directly in such fluids (e.g., Fusswinkel et al., 2017; Rauchenstein-Martinek et al., 2014, 2016). A lack of such studies partly reflects the petrographic and temporal complexity, and often poor inclusion preservation—simply the consequence of prolonged fluid flux and protracted deformation histories that characterize these systems (e.g., Kontak & Tuba, 2017; Ridley & Diamond, 2000; Ridley & Hagemann, 1999; Tuba et al., 2021).

The preservation of undeformed quartz euhedra hosting texturally unambiguous populations of remarkably large and well-preserved fluid inclusions allows for the aforementioned problems noted for OGD to be circumvented. Type 1a fluid inclusions, interpreted as the earliest fluid preserved in the Dufferin saddle veins, have

compositional characteristics consistent with studies over the past several decades indicating a prevalence of low-salinity (<10 wt.% NaCl equiv.), near-neutral pH, aqueous-carbonic (X_{CO_2} = 0.05–0.15) Au-mineralizing fluids responsible for the formation of OGD (e.g., Bodnar et al., 2014; Fusswinkel et al., 2017; Goldfarb & Groves, 2015; McCuaig & Kerrich, 1998; Ridley & Diamond, 2000; Roedder, 1984). Of relevance is that similar fluids (Figure 7a) are also recognized in mineralized auriferous magmatic-hydrothermal environments (e.g., deep Cu-Au porphyry: Reed et al., 2013; Rusk, Reed, Dilles, et al., 2004, intrusion-related gold systems: Mair et al., 2006; Marsh et al., 2003; Lang & Baker, 2001; Thompson et al., 1999). Importantly, such fluid compositions are characteristic of both Au-enriched and Au-barren metamorphic terrains (Marsala et al., 2013; Miron et al., 2013; Rauchenstein-Martinek et al., 2014, 2016; Figure 7a). Thus, the low salinity, near-neutral, aqueous-carbonic nature of fluid compositions in OGD systems can result from common crustal processes and are not a hallmark of Au-mineralizing potential in OGD environments. Rather, the potential for such fluids to yield high-grade OGD deposits must reflect the availability of Au (from anomalously Au-enriched source rocks or coeval magmas that exsolve Au-bearing volatiles) and/or efficient processes of gold transport and precipitation, in addition to later potential upgrading related to metal mobilization (e.g., Choquette et al., 2023; Hastie et al., 2020) or overprinting events (Kerr et al., 2018).

The range in P-T conditions associated with vein emplacement is in part constrained by the entrapment of aqueous-carbonic fluids in secondary domains of quartz (i.e., CDP structures). Importantly, the latter record conditions fall below those corresponding to peak regional metamorphism in this part of the Meguma terrane (i.e., lower greenschist) and the thermal effects of the contact aureole of the distal (i.e., 20 km) ca. 380 Ma Musquodoboit Batholith, which is estimated to be emplaced ca. 4.2 ± 0.5 kbars (see above). The maximum temperature of type 1 and type 2 fluid inclusion entrapment is estimated at 300 ± 30°C, while the pressures of entrapment (at 330°C) are constrained to between ∼0.5 and 3 kbar based on isochores (Figure 6). From this, it is implicit that fluid depressurization must have occurred during vein formation, which is likely related to transient fluid pressure fluctuations from lithostatic to hydrostatic conditions and commensurate with formation of crack-seal textured veins (e.g., fault valve model; Sibson et al., 1988). Such pressure cycling will also lead to periods of elevated quartz solubility if the appropriate P-T-pH space is intersected in the H_2O-CO_2-NaCl system (e.g., Crundwell, 2017; Li et al., 2020; Monecke et al., 2018, 2019). While common in other hydrothermal settings (Mao et al., 2017; Monecke et al., 2018; Steele-MacInnis et al., 2012; Sun et al., 2020), quartz solubility behavior in the H_2O-CO_2-NaCl has only been recently modeled and applied to porphyry (Monecke et al., 2019) and OGD (Li et al., 2020) settings. Although there is a complex relationship between quartz solubility and intensive parameters (i.e., P-T), as well as with fluid chemistry (i.e., NaCl, CO_2, and hydrocarbons), a dramatic increase in quartz solubility can occur upon fluid immiscibility due to isobaric cooling or isothermal decompression (Li et al., 2020; Steele-MacInnis et al., 2012). Furthermore, and relevant to Dufferin, the rate of quartz dissolution in aqueous fluids is enhanced with both increasing pH (i.e., pH ≥ ∼6; Crundwell, 2017) and dissolved organic compounds (e.g., carbonaceous/bituminous material; Bennett & Siegel, 1987). The presence of chemical etching on the quartz crystal surfaces (e.g., Figure 2f) may relate to these aforementioned parameters. Additionally, the latter is relevant to the generation of porosity (enhanced by fluid pH modification and the presence of hydrocarbons) during which time causative fluids could not be trapped as quartz was in a state of dissolution. Subsequent cooling and depressurization would have resulted in reentry of the system into a state of active quartz precipitation that resulted in the formation of secondary quartz domains hosting auriferous type 1 and type 2 fluids (Figure 4d).

The similarity between the relative abundances of carbonic phase-hosted volatile species (i.e., CO_2, CH_4, and N_2; Figures 5a and 5j) and the speciation of dissolved components in the aqueous phases (i.e., $B(OH)_3$, HCO_3^- and $CO_{2(aq)}$; Figure 5k) of type 1a and 1b inclusions suggests they are genetically related (i.e., that one evolved from the other). Variations in bulk salinity (Figure 8c) between type 1a and 1b inclusions (i.e., <2 and 4 to 5.2 wt. % NaCl equiv., respectively) are interpreted to reflect changes in fluid composition with time due to fluid-rock interaction. However, the variation in the vapor phase density between types 1a and 1b inclusions likely reflects pressure fluctuation during fluid entrapment within the single-phase field (Figure 6), a feature of OGD settings in general (Diamond, 2001; Schmidt & Bodnar, 2000). In addition, decreasing fluid X_{CO_2} (Figure 8a) and increasing aqueous phase salinity (Figure 8b) over the transition from type 1a to 1b fluids likely occurred through carbonate precipitation and fluid dehydration due to wallrock interaction. The change in salinity related to fluid/rock interaction is further supported by the LA-ICP-MS data (Table S3), which shows that type 2 inclusions are relatively enriched in wallrock-inherited, and chloride-ligated elements (Mg, Ca, Sr, and possibly Fe).
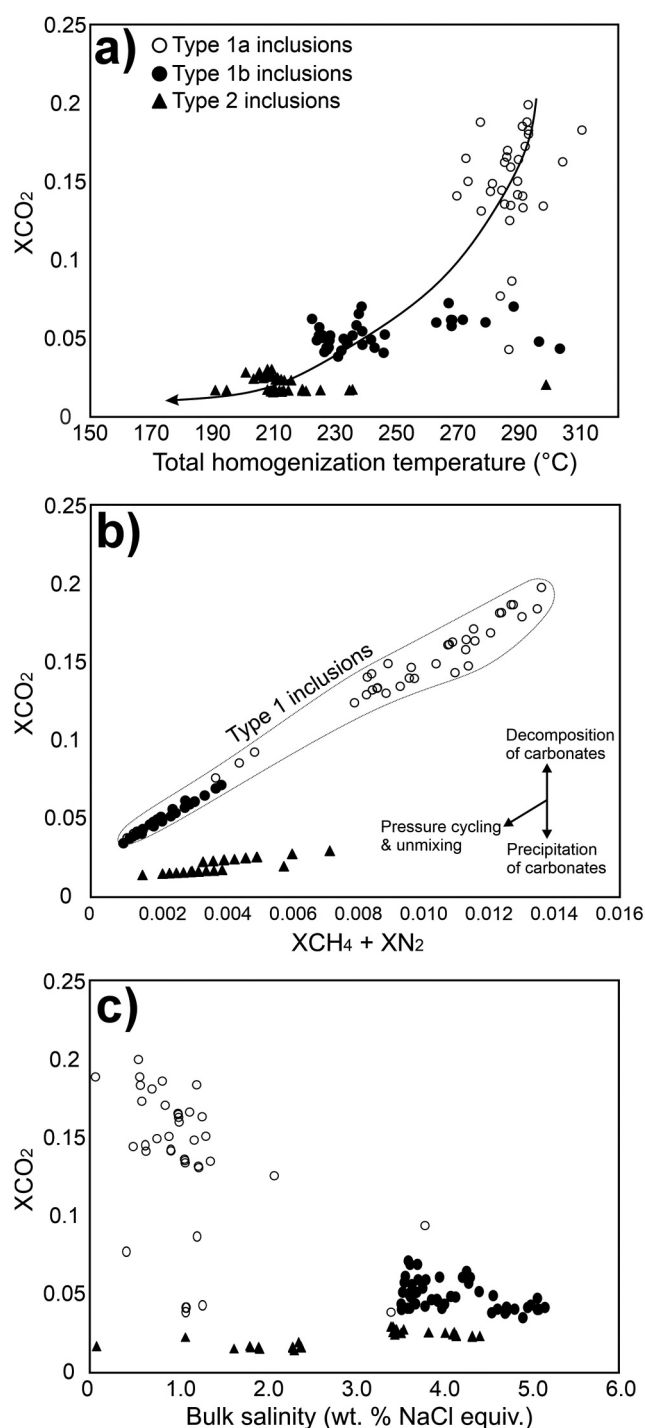
Figure 8. Microthermometric and bulk compositional data for all fluid inclusion types (from saddles 3 and 6). (a) Bulk CO_2 abundance versus fluid inclusion total homogenization temperature. A decrease in total homogenization temperature with decreasing CO_2 abundance is observed from type 1 to type 2 inclusions (black line). (b) Bulk $[CH_4 + N_2]$ abundance vs. bulk CO_2 abundance. Type 1a and 1b inclusions share a consistent CO_2/$[CH_4+N_2]$ ratio. (c) Bulk CO_2 abundance versus bulk fluid inclusion salinity (wt.% NaCl equiv.).

Consistent bulk densities and consequently overlapping isochoric fields among all inclusion types suggest that the observed decrease in Th_{TOT} with decreasing bulk X_{CO2} (Figure 8a) reflects contraction of the immiscibility (2-phase) field to lower T as the bulk $CO_2(\pm CH_4+N_2)$ of the fluid decreases (Diamond, 2003). Therefore, carbonate may have precipitated from a homogeneous fluid (e.g., type 1a fluid) at higher P-T conditions (~270–310°C, 2–3 kbar), reducing the (bulk) fluid CO_2 and maintaining fluid homogeneity to lower P-T conditions (~190°–300°C, 1–2 kbar). Lastly, it is noted that type 2 inclusions show a distinct vapor phase volatile chemistry and bulk CO_2/$(CH_4 + N_2)$ values relative to type 1 inclusions. The high abundance of CH_4 and N_2 observed in the vapor phase of type 2 fluid inclusions would result from carbonate precipitation, and commensurate CO_2 removal from type 1 fluid. In addition, fluid equilibration with the organic-rich slates of the country rocks (e.g., Glasmacher et al., 2003; Kerr et al., 2021) may also contribute N_2 and CH_4, as these volatiles can be readily produced via the decomposition/devolatilization of organic matter present in the sedimentary protoliths (Beaumont & Robert, 1999), with additional N_2 potentially from the decomposition of NH_4^+-bearing phyllosilicates (Glasmacher et al., 2003; Papineau et al., 2005).

5.3. Gold Precipitation During Fluid-Rock Interaction and Related Chemical Parameters

Studies in recent years have shown that gold enrichment in OGD settings likely reflects protracted periods of primary enrichment by a variety of processes (e.g., fluid unmixing, wall-rock sulfidation; Craw et al., 1993; Dubosq et al., 2018; Fougerouse et al., 2017; Herzog et al., 2024; Lawley et al., 2017; Naden & Shepherd, 1989; Neumayr & Hagemann, 2002; Neyedley et al., 2017; Olivo & Williams-Jones, 2002) and subsequent remobilization and upgrading of earlier gold tenors through processes involving aqueous (Hastie et al., 2020; Kerr et al., 2018; Voisey et al., 2019) and/or colloidal gold (Hastie et al., 2021; McLeish et al., 2021; Williams-Jones et al., 2009). Many mechanisms are suggested for gold precipitation in OGD settings, but in all cases these involve the destabilization of aqueous Au complexes (e.g., Gaboury, 2019; Renders & Seward, 1989; Seward, 1973; Shenberger & Barnes, 1989; Williams-Jones et al., 2009 and references therein). Of particular relevance here are settings in which gold formation/precipitation has ostensibly resulted from fluid reduction via interaction with CM (Table 1). At Dufferin, interaction of auriferous fluid(s) with CM hosted in the wallrock (i.e., black slates) and/or fragments of earlier laminated parts of the quartz veins (i.e., Figure 2b) lead to fluid reduction and concomitant destabilization of Au-bisulfide complexes. Evidence of this is the common textural association of coeval μm-sized gold particles and CM in CM-lined cavities/grain boundaries (Figure 3e). The influence of CM on gold solubility is familiar to industry (Breerwood, 1938; Scheiner, 1971), with electrochemical studies showing an inverse correlation between CM abundance with gold oxidation and dissolution (van Deventer et al., 2005). Furthermore, precipitation of gold onto the surfaces of CM particles likely occurred locally via adsorption/chemisorption, analogous to the "preg-robbing" mechanism in which dissolved Au in cyanide leachates is adsorbed onto CM, which leads to decreased gold recovery during ore processing (cf., Miller et al., 2005; Vaughan, 2004), a process that is more efficient involving CM of lower maturity and higher degree of disorder (i.e., bitumen/pyrobitumen compared to graphite).

The solubility of Au as a neutral bisulfide species at temperatures ≤350°C is described by Equation 1 and predicts that a decrease in fluid $f\mathrm{O}_2$ and/or an increase in pH cause(s) Au precipitation (Gibert et al., 1998; Renders & Seward, 1989; Seward, 1973; Shenberger & Barnes, 1989; Stefánsson & Seward, 2004).

$$\mathrm{Au(HS)^0 + \tfrac{1}{2}H_2O = Au_{(s)} + HS^- + H^+ + \tfrac{1}{4}O_2} \tag{1}$$
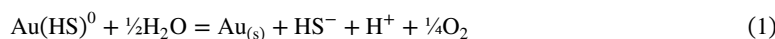
Aqueous-carbonic fluids, formed through magmatic devolatilization and/or country rock dehydration and decarbonation reactions have favorable physicochemical properties for Au transport via bisulfide complexing (i.e., near-neutral to slightly acidic pH of ∼4–6, mildly oxidizing to reducing $f\mathrm{O}_2$, and T < 350°C; Wood & Samson, 1998 and references therein; Williams-Jones et al., 2009). Raman spectra from the CM in association with gold indicate that the CM was heated to temperatures of approximately 300 ± 30°C, which provides a minimum temperature for quartz vein formation and a maximum temperature for Au deposition in association with CM. Gold-bearing fluids that have interacted with the CM during fluid migration through the permeable lithologies and/or faults/fractures would be strongly reduced to a level corresponding to the graphite-COH buffer (Equations 2 and 3).

$$\mathrm{C + O_2 = CO_2} \tag{2}$$

$$\mathrm{2C + 2H_2O = CO_2 + CH_4} \tag{3}$$

Furthermore, if fluids generated during prograde regional metamorphism at depth and/or from the thermal aureoles around related underlying intrusive bodies ascend to higher crustal levels, cooling of the fluid likely occurred (Goldfarb & Groves, 2015). In open systems, a decrease in $X\mathrm{CO_2}/(X\mathrm{CH_4} + X\mathrm{CO_2})$ is observed with decreasing temperatures (Figure 8a; Huizenga & Touret, 1999) as oxygen fugacity is buffered at progressively lower values during cooling (Huizenga, 2001; Huizenga & Touret, 1999; Ulmer & Luth, 1991) and is negligibly influenced by desulfidation of wallrocks at low to medium metamorphic grades (Connolly & Cesare, 1993). At Dufferin, relevant buffering lithologies within the Meguma Group include variably carbonaceous (i.e., <1–10% organic carbon) black slates/shales (Graves & Zentilli, 1988; Waldron, 1992).

Evidence for fluid reduction at Dufferin is provided by the significant decrease in concentrations of the redox-sensitive semi-metals As and Sb with decreasing Au concentration in the fluid (Figures 7c and 7d), in addition to the enrichment of As and Sb in the temporally earlier type 1a inclusions relative to later type 2 inclusions (i.e., 2—5x enrichment factor; Figure 7a). Rather than as chlorides, these metals are mobilized in low salinity hydrothermal fluids primarily as metal hydroxides [e.g., $\mathrm{Sb^{3+}(OH)_3}$, $\mathrm{As^{3+}(OH)_3}$, $\mathrm{H_3As^{5+}O_4}$] or thiolates [e.g., $\mathrm{Sb(HS)_4^-}$, $\mathrm{Sb(HS)_{4-n}(OH)_n^-}$, $\mathrm{As(OH)(SH)_2^0}$], although the stoichiometry of aqueous Sb and As thiolates are poorly understood, and are believed to dominate only in fluids with high dissolved sulfide concentrations (O'Day, 2006; Sherman et al., 2000; Wood & Samson, 1998 and references therein). Thus, their dissolved concentrations are not strongly influenced by fluid salinity (i.e., chlorinity). Considering As specifically, recent work modeling As + Au-enrichment in ores by hydrothermal fluids at T < 300°C showed that fluids with low As concentrations are capable of precipitating arsenian pyrite and arsenopyrite (as are observed in late fractures associated with CM in this study; Figure 3d) by reduction during prolonged fluid-rock interaction at relatively high fluid/rock ratios (Xing et al., 2019). This is consistent with earlier work that showed that a ∼4 order of magnitude reduction in fluid $f\mathrm{O}_2$ in the Fe-As-S-O-H system at 250°C causes the destabilization of aqueous $\mathrm{As^{3+}(OH)_3}$ (i.e., decomposition and precipitation of arsenopyrite (Heinrich & Eadington, 1986; Figure 9)).

It is therefore posited that during migration of auriferous fluids through the crust, cooling and interaction with CM-bearing lithologies led to the reduction of $\mathrm{Au^+}$, destabilization of aqueous Au bisulfide species, and Au precipitation via Equation 4 (e.g., Hu et al., 2017), explaining the close textural association between CM and Au (Figures 3e and 3f):

$$\mathrm{4\big[Au(HS)_2\big]^-_{(aq)} + C_{(s)} + 2H_2O + 4H^+ = 4Au_{(s)} + CO_2 + 8H_2S_{(aq)}} \tag{4}$$

Auriferous vein carbonates at the Dufferin deposit and other Meguma-type deposits have very low values of $\delta^{13}\mathrm{C}_{\mathrm{VPDB}}$ (this study: $\delta^{13}\mathrm{C}_{\mathrm{VPDB}} = -21.1‰$ and $-21.3‰$; Kontak & Kerrich, 1997: avg. $\delta^{13}\mathrm{C}_{\mathrm{VPDB}} = -22.3‰$, $n = 3$) and is consistent with vein C being sourced from the decomposition of sedimentary organic matter (e.g.,
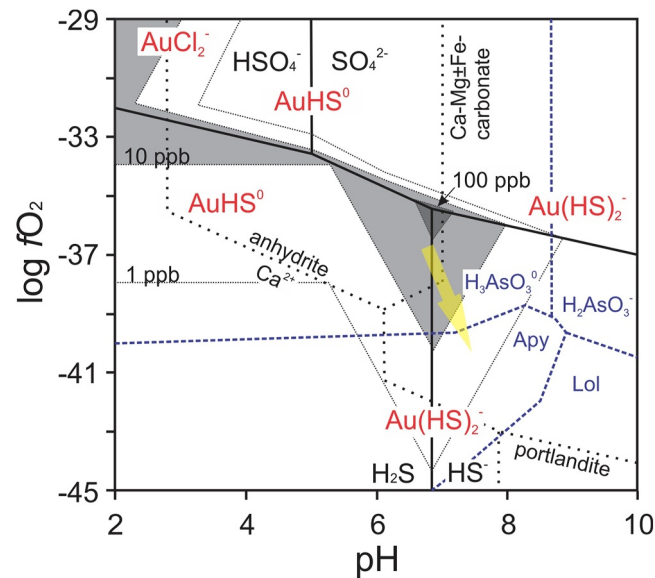
Figure 9. Log fO_2—pH diagram relevant to the Dufferin deposit. The inferred fluid evolution pathway (yellow arrow) in the log fO_2—pH space associated with the precipitation of Au (cf., Williams-Jones et al., 2009: 0.5 kbar and 250°C in an aqueous solution of 1 m NaCl and 0.01 m ΣS), arsenopyrite (cf., Heinrich & Eadington, 1986: 250°C in Fe-As-S-O-H-bearing aqueous fluid), and carbonates. Carbonate stability fields were modeled using Geochemist's Workbench (Aqueous Solutions LLC) Act2 platform: 1 kbar and 250°C in an aqueous solution with $a_{H2O} = 1$, $a_{Ca2+} = 0.00825$ (using activity coefficient of ~0.3 based on a fluid ionic strength of 0.188; cf., Garrels & Christ, 1965), $a_{S\ total} = 0.01$, $a_{Cl-} = 0.1$, $a_{Na+} = 0.1$, a_{Mg2+} of 0.0001, and $a_{HCO3-} = 0.0005$. Aqueous sulfur species and carbonate species were allowed to speciate over the log fO_2 and pH range specified.

Jurisch et al. (2012)). The oxidation of CM in Meguma lithologies at depth would produce ^{13}C-depleted CO_2 (i.e., Equations 2 and 3) and subsequent aqueous carbonate and bicarbonate that combine with $Ca^{2+}_{(aq)}$ ($\pm Mg^{2+}_{(aq)}$), leached from wallrock detrital silicates, would produce calcite and dolomite (Sangster, 1992) with predictably very low $\delta^{13}C_{VPDB}$ values (Equation 5).

$$CaCl_{2(aq)} + H_2O + CO_2 = CaCO_{3(s)} + 2H^+ + 2Cl^- \tag{5}$$
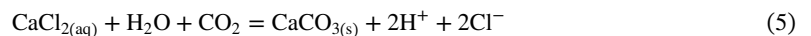
Given the inferred temperature of vein formation (300°–400°C) and CO_2-rich nature of the fluids, $\delta^{13}C_{carbonate} \approx \delta^{13}C_{H2CO3} \approx \delta^{13}C_{CO2}$ and therefore the low $\delta^{13}C$ signature is a primary feature of the fluid (cf., Kontak & Kerrich, 1997). Thus, production of an auriferous aqueous-carbonic fluid via dehydration and decarbonation of country rocks at depth (i.e., source) can lead to the precipitation of gold and carbonates at shallower crustal levels (i.e., sink) as a result of subsequent fluid cooling and reduction. Equation 6, resulting through combination of Equations 4 and 5, demonstrates a chemical pathway by which soluble gold bisulfide and CM are respeciated at the sink site, resulting in the precipitation of gold and carbonate.

$$4[Au(HS)_2]^-_{(aq)} + CaCl_{2(aq)} + C_{(s)} + 3H_2O + 2H^+ \leftrightarrow 4Au_{(s)} + CaCO_{3(s)} + 8H_2S_{(aq)} + 2Cl^- \tag{6}$$
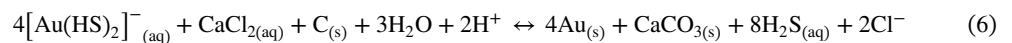
In this way, CO_2 can be considered as a chemically transient phase, facilitating the transport of gold in a fluid by promoting favorable physicochemical characteristics (e.g., near-neutral pH). Carbon dioxide, present as aqueous CO_2 and bicarbonate in the fluid (see Figure 5), plays a critical role in Au transportation by buffering the pH of the fluid in a range where Au bisulfide complexes remain soluble (Phillips & Evans, 2004). Therefore, removal of CO_2 through the precipitation of carbonates or through localized precipitation of CM (i.e., hydrothermal graphite; Equation 7; Hu et al., 2017; Kendrick et al., 2011) would influence the pH of the fluid and destabilize soluble Au bisulfide complexes.

$$8AuHS^0_{(aq)} + 3CO_2 + 5CH_4 = 8Au_{(s)} + 8C_{(s)} + 8H_2S_{(aq)} + 6H_2O \tag{7}$$
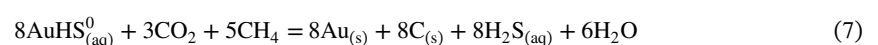
This mass action expression (Equation 7) is driven to the right during cooling (≤350°C), during which time graphite precipitation is predicted for initially graphite-undersaturated fluids (Cesare, 1995; Huizenga, 2001).

Importantly, the late aqueous-carbonic fluids from mineralized Dufferin saddle veins are: (a) Au-undersaturated ($[Au]_{avg} = 0.045$ ppm in type 1a fluid vs. $[Au]_{calc.} \approx 0.1$–2 ppm or $[Au]_{calc.} \approx 5 \times 10^{-7}$—$1 \times 10^{-5}$ mol/kg at 300°C); and (b) S-saturated ($[S]_{avg} = \sim330$ ppm in type 1a inclusions vs. $[S]_{calc.} \approx 30$–320 ppm or $[S]_{calc.} \approx 0.01$–0.001 mol/kg at 300°C) with respect to concentrations predicted in H_2O-CO_2-H_2S-NaCl-bearing hydrothermal fluids with similar compositions (Rauchenstein-Martinek et al., 2014). This suggests that the capacity of a fluid to mobilize Au is not necessarily a function of Au and S solubility, but rather the labile nature of Au in the source region and/or causative magmatic intrusions (e.g., Rauchenstein-Martinek et al., 2014). The Au concentration in type 1a fluid is comparable to geochemically similar Alpine fluids of inferred metamorphic origin hosted in Au-barren veins (i.e., $[Au] \approx 0.03$–0.11 ppm; Rauchenstein-Martinek et al., 2014, 2016). Therefore, late Au mineralization at Dufferin likely reflects a highly efficient precipitation mechanism(s) that is/are absent in barren orogenic systems involving similarly Au-enriched fluids.

5.4. Implications for the Origin of the Auriferous Vein-Forming Fluids at Dufferin

The origin of Au-mineralizing aqueous-carbonic fluids in metamorphic terranes continues to be enigmatic (Goldfarb & Groves, 2015; Goldfarb et al., 2005; Groves et al., 2003, 2024). Numerous studies have shown that aqueous-carbonic fluid compositions, including their volatile constituents (e.g., CO_2, CH_4, N_2) and fluid salinity, are similar in both intrusion-related (Lang & Baker, 2001; Thompson et al., 1999) and orogenic (Bodnar et al., 2014; McCuaig & Kerrich, 1998; Ridley & Diamond, 2000) gold settings. Furthermore, the timing of fluid entrapment is poorly constrained because unequivocal identification of primary quartz-hosted fluid inclusions (i.e., confined to growth zones) in OGD samples and unmineralized metamorphic equivalents are rarely reported (Bons et al., 2012; Rauchenstein-Martinek et al., 2014; Van den Kerkhof & Hein, 2001; Zoheir et al., 2019).

At Dufferin, the timing of saddle vein formation is constrained by two independent but related parameters: absolute age dating and a robust structural model of vein emplacement. With respect to the former, Re-Os dating of vein-hosted arsenopyrite yielded coincident isochron and model ages of 380 Ma (Morelli et al., 2005) that support an earlier $^{40}Ar/^{39}Ar$ age of ~380 Ma (Kontak & Archibald, 2002; Kontak et al., 1998). These dates are consistent with the proposed structural model for Meguma gold vein formation (Horne & Culshaw, 2001; Kontak & Horne, 2010), and Dufferin in particular (Horne & Jodrey, 2001), whereby fold tightening in response to emplacement of the large granitoid intrusions at ~380 Ma (Figure 1a), and development of flexural slip planes localized formation of the laminated and saddle-reef veins. In this model, vein fluids are plausibly derived from: (a) exsolution of volatiles from cooling of unexposed granitoid intrusion(s) at depth, similar to those currently exposed in the Meguma terrane (i.e., South Mountain and Musquodoboit Batholiths; Figure 1a); and/or (b) dehydration and decarbonation of country rocks in the contact aureoles of the same putative cooling intrusion (e.g., Kempe et al., 2016; Figure 10). The latter thus accommodates relative and absolute timing of gold deposit formation to syn-granite emplacement, and thus relatively late with respect to regional metamorphism and deformation as reviewed above.

Based on the metal contents of the Dufferin fluid inclusions, a distinction cannot be made with respect to the Au source. A review of the compositions of ore fluids from over 19 deposits of magmatic-hydrothermal and metamorphic affinity (Figure 7a) shows that with respect to major-, minor- and trace-element concentrations, there are unfortunately no reliable elemental discriminators. For example, enrichment in B-As-Sb-Au, such as that observed in type 1a fluid inclusions at Dufferin, has been variably interpreted as evidence for a magmatic origin, as these elements are preferentially enriched in magmatic vapors during boiling in magmatic-hydrothermal systems (Heinrich et al., 1999; Williams-Jones & Heinrich, 2005, and references therein). However, it remains equivocal whether such B-As-Sb-Au-enriched fluids originate from deeply intruded S-type granitoids, such as the nearby Musquodoboit Batholith (Figure 1), or from fluid interaction with metalliferous metasedimentary country rocks (e.g., Meguma terrane; White & Goodwin, 2011). Available data indicate that rocks of the Meguma stratigraphy are depleted in Sb but moderately enriched in As (e.g., Beaverbank Formation of the upper part of the Goldenville Group: <0.1–0.4 ppm Sb vs. 5–75 ppm As in whole rock assays; White & Goodwin, 2011), which suggests a possible local contribution of As to the ore fluid through fluid/rock interaction. However, an increase in the presence of arsenopyrite (also chalcopyrite, galena, and sphalerite) in contact aureoles proximal to the granitic South Mountain Batholith (Clarke et al., 2009) suggests a possible magmatic metal input related to this regional
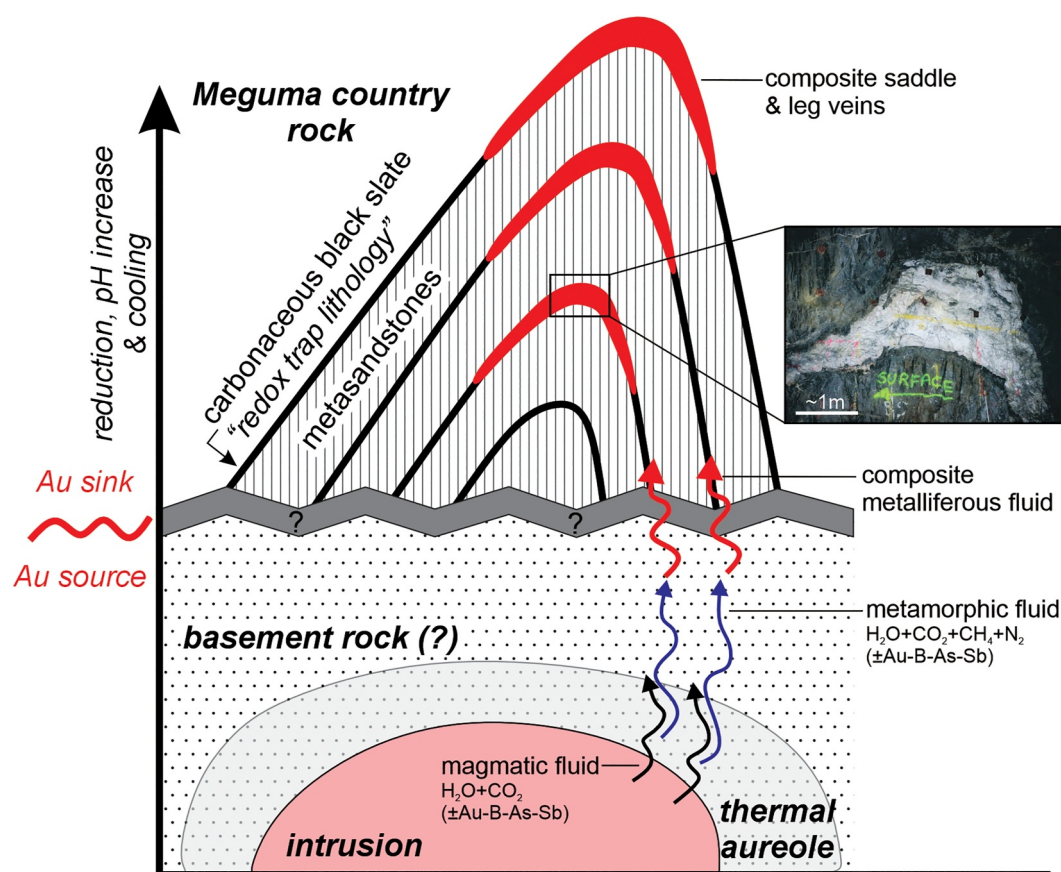
Figure 10. Schematic for gold precipitation at Dufferin. This schematic model (not to scale) involves fluid generation by magmatic devolatilization and/or dehydration-decarbonation through thermal metamorphism in basement rocks at depth, yielding an Au-endowed composite fluid that migrates to shallower crustal levels (i.e., into Meguma country rocks). The auriferous fluid is subjected to cooling, reduction and pH modification through interaction with organic-rich lithologies, in this case the Dufferin setting, and subsequent precipitation of gold in the "Au sink" region.

magmatic event. Additionally, Au positively correlates with As + Sb in type 1a fluid inclusions and late-stage arsenopyrite mineralization is present in fractures (Figure 3d) in auriferous quartz veins.

The source of Au in Meguma deposits is still equivocal, with both magmatic and country rock-derived sources debated (Kontak & Kerrich, 1997; Kontak & Kyser, 2011; Kontak & Smith, 1989; Kontak et al., 1990, 1998, 2011, 2012; Morelli et al., 2005; Ryan & Smith, 1998). Additionally, Sangster (1992) argued that Au may have been remobilized from the anoxic carbonaceous sedimentary rocks of the Goldenville Group which, in the context of the present study, suggests CM-bearing lithologies may act as both a Au source and sink (e.g., Large et al., 2011; Figure 10). Regardless of the ultimate source of Au, it is well documented that vein-forming fluids associated with Au deposits in the Meguma terrane interact with their country rocks (Kontak & Kerrich, 1997; Kontak et al., 2011). For instance, vein carbonate $\delta^{13}C_{VPDB}$ values overlap with those for diagenetic carbonate and graphite in Goldenville Group metasedimentary rocks (-13 to $-22‰$; Kontak & Kerrich, 1997). At Dufferin, late hydrothermal carbonate from saddle 6 (Figure 2d) is similarly ^{13}C-depleted ($\delta^{13}C_{VPDB} = -21.1‰$ and $-21.3‰$). Therefore, carbonic species in the ore fluid at Dufferin were likely derived from organic-bearing country rocks. Furthermore, the $\delta^{34}S_{sulfide}$ values for sulfides from the Meguma Au deposits mimic the general upward increase in $\delta^{34}S_{suldfide}$ values seen in the Meguma Group stratigraphy (Kontak & Smith, 1989; Sangster, 1992), which suggests a strong S contribution by the wallrocks. Thus, even with the new data generated in this study and that of previous workers, it is apparent that the discrimination of fluid reservoirs remains challenging.

6. Conclusions

This study presents one of few data sets for Au and associated metal and sulfur concentrations in aqueous-carbonic fluid inclusions in an OGD setting, albeit of secondary nature with respect to some, but not all, of the vein quartz, considered to be part of the multi-stage gold-mineralizing event. The composition of these fluids, including Au content (~20–50 ppb), is comparable to poorly mineralized quartz vein systems elsewhere (Rauchenstein-Martinek et al., 2016), thus highlighting the necessity of documenting the process(es) responsible for Au mineralization. At Dufferin, despite auriferous fluid inclusions being secondary in origin, several features suggest that their compositions represent, at least in part, the range of fluids responsible for Au deposition, including their occurrence with Au-bearing veins, bulk compositions and homogenization temperatures consistent with other OGD, and their metal contents (including Au). The lack of preservation of primary fluid inclusions throughout the entirety of the Au-forming hydrothermal system at Dufferin makes these secondary fluid inclusions the best opportunity to characterize the fluids responsible for Au mineralization in these deposits. Moreover, this study documents the importance of CM as a factor in one of several efficient processes responsible for controlling Au mineralization. The results of this study are integrated with previous work on Meguma Au deposits to suggest a revised genetic model (Figure 10) including: (a) production of an auriferous, yet gold-undersaturated fluid through combined magmatic devolatilization, and/or country rock dehydration and decarbonation mechanisms related to contact metamorphism; (b) migration and focusing of this fluid into anticlinal hinge structures containing reducing lithologies (e.g., CM-bearing black slate or argillite); and (c) precipitation of gold, and other metals, via coupled reduction-pH increase as this fluid reacts with CM-bearing lithologies. In particular, careful measurement of the composition of fluid inclusion types documents an evolution of fluid chemistry consistent with decreasing fO_2 and increasing pH, which led to in situ precipitation of gold + carbonate + arsenopyrite ± CM. Importantly, findings support previous work suggesting a genetic link between Au and CM in other settings worldwide, such as the western Lachlan orogeny, Carlin deposits, and Ashanti gold belt, for example.

Data Availability Statement

All data collected for this study and referenced herein are currently available as three supplemental documents: Tables S1 through Table S3. These tables are open and available as per AGU's FAIR Data guidelines on *Borealis: The Canadian Dataverse Repository* in the Saint Mary's University Dataverse via Kerr (2024).

References

Bakker, R. J. (1999). Adaptation of the Bowers and Helgeson (1983) equation of state to the H$_2$O–CO$_2$–CH$_4$–N$_2$–NaCl system. *Chemical Geology*, *154*, 225–236.

Bakker, R. J. (2003). Package FLUIDS 1. Computer programs for analysis of fluid inclusion data and for modeling bulk fluid properties. *Chemical Geology*, *194*(1–3), 3–23. https://doi.org/10.1016/s0009-2541(02)00268-1

Beaumont, V., & Robert, F. (1999). Nitrogen isotope ratios of kerogens in Precambrian cherts: A record of the evolution of atmosphere chemistry? *Precambrian Research*, *96*(1–2), 63–82. https://doi.org/10.1016/s0301-9268(99)00005-4

Beeskow, B., Rankin, A. H., Murphy, P. J., & Treloar, P. J. (2005). Mixed CH$_4$-CO$_2$ fluid inclusions in quartz from the South Wales Coalfield as suitable natural calibration standards for microthermometry and Raman spectroscopy. *Chemical Geology*, *223*(1–3), 3–15. https://doi.org/10.1016/j.chemgeo.2005.01.028

Benn, K., Horne, R. J., Kontak, D. J., Pignotta, G., & Evans, N. G. (1997). Syntectonic emplacement of the South Mountain Batholith, Meguma Terrane, Nova Scotia: Magnetic fabric and structural analyses. *Bulletin of the Geological Society of America*, *109*(10), 1279–1293. https://doi.org/10.1130/0016-7606(1997)109<1279:saemft>2.3.co;2

Bennett, P., & Siegel, D. I. (1987). Increased solubility of quartz in water due to complexing by organic compounds. *Nature*, *326*(6114), 684–686. https://doi.org/10.1038/326684a0

Berge, J. (2011). Paleoproterozoic, turbidite-hosted, gold deposits of the Ashanti gold belt (Ghana, West Africa): Comparative analysis of turbidite-hosted gold deposits and an updated genetic model. *Ore Geology Reviews*, *39*(1–2), 91–100. https://doi.org/10.1016/j.oregeorev.2010.12.001

Bickerton, L., Kontak, D. J., Murphy, J. B., Kellett, D. A., Samson, I. M., Marsh, J. H., et al. (2022). The age and origin of the South Mountain Batholith (Nova Scotia, Canada) as constrained by zircon U–Pb geochronology, geochemistry, and O–Hf isotopes. *Canadian Journal of Earth Sciences*, *59*(7), 418–454. https://doi.org/10.1139/cjes-2021-0097

Bierlein, F. P., Cartwright, I., & McKnight, S. (2001). The role of carbonaceous "indicator" slates in the genesis of lode gold mineralization in the Western Lachlan orogen, Victoria, Southeastern Australia. *Economic Geology*, *96*(3), 431–451. https://doi.org/10.2113/gsecongeo.96.3.431

Bierlein, F. P., & Smith, P. K. (2003). The Touquoy Zone deposit: An example of "unusual" orogenic gold mineralization in the Meguma Terrane, Nova Scotia, Canada. *Canadian Journal of Earth Sciences*, *40*(3), 447–466. https://doi.org/10.1139/e03-002

Bodnar, R. J. (2003). Introduction to fluid inclusions. In I. Samson, A. Anderson, & M. Marshall (Eds.), *Fluid inclusions: Analysis and interpretation* (pp. 1–8). Mineralogical Association of Canada Short Course.

Bodnar, R. J., Lecumberri-Sanchez, P., Moncada, D., & Steele-MacInnis, M. (2014). Fluid inclusions in hydrothermal ore deposits. In *Reference module in Earth systems and environmental sciences treatise on geochemistry* (2nd ed., pp. 119–142).

Bodnar, R. J., & Vityk, M. O. (1994). Interpretation of microthermometric data for H_2O-NaCl fluid inclusions. In B. De Vivo & M. L. Frezzotti (Eds.), *Fluid inclusions in minerals, methods, and applications* (pp. 117–130).

Bons, P. D., Elburg, M. A., & Gomez-Rivas, E. (2012). A review of the formation of tectonic veins and their microstructures. *Journal of Structural Geology*, *43*, 33–62. https://doi.org/10.1016/j.jsg.2012.07.005

Bowers, T. S., & Helgeson, H. C. (1983). Calculation of the thermodynamic and geochemical consequences of nonideal mixing in the system H_2O-CO_2-NaCl on phase relations in geologic systems: Equation of state for H_2O-CO_2-NaCl fluids at high pressures and temperatures. *Geochimica et Cosmochimica Acta*, *47*(7), 1247–1275. https://doi.org/10.1016/0016-7037(83)90066-2

Breerwood, C. H. (1938). US Patent No. 2130574. In *Flotation of carbonaceous ore*.

Cesare, B. (1995). Graphite precipitation in C-O-H fluid inclusions: Closed system compositional and density changes, and thermobarometric implications. *Contributions to Mineralogy and Petrology*, *122*(1–2), 25–33. https://doi.org/10.1007/s004100050110

Choquette, B., Kontak, D. J., Côté-Lavoie, É., & Fayek, M. (2023). A fluid chemical study of the world-class, intrusion-related archean windfall gold deposit, Quebec, Canada. *Economic Geology*, *118*(6), 1397–1429. https://doi.org/10.5382/econgeo.5033

Clarke, D. B., Erdmann, S., Samson, H., & Jamieson, R. A. (2009). Contamination of the South Mountain Batholith by sulfides from the country rocks. *The Canadian Mineralogist*, *47*(5), 1159–1176. https://doi.org/10.3749/canmin.47.5.1159

Clarke, D. B., MacDonald, M. A., & Tate, M. C. (1997). Late Devonian mafic-felsic magmatism in the Meguma zone, Nova Scotia. In A. K. Sinha, J. F. Whalen, & J. P. Hogan (Eds.), *The nature of magmatism in the appalachian orogen* (Vol. 191, pp. 107–127). Geological Society of America Memoir. https://doi.org/10.1130/0-8137-1191-6.107

Connolly, J. A. D., & Cesare, B. (1993). C-O-H-S fluid composition and oxygen fugacity in graphitic metapelites. *Journal of Metamorphic Geology*, *11*(3), 379–388. https://doi.org/10.1111/j.1525-1314.1993.tb00155.x

Craw, D. (2002). Geochemistry of late metamorphic hydrothermal alteration and graphitization of host rock, Macraes gold mine, Otago Schist, New Zealand. *Chemical Geology*, *191*(4), 257–275. https://doi.org/10.1016/s0009-2541(02)00139-0

Craw, D., Teagle, D. A. H., & Belocky, R. (1993). Fluid immiscibility in late-Alpine gold-bearing veins, Eastern and Northwestern European Alps. *Mineralium Deposita*, *28*(1), 28–36. https://doi.org/10.1007/bf00199007

Crundwell, F. K. (2017). On the mechanism of the dissolution of quartz and silica in aqueous solutions. *ACS Omega*, *2*(3), 1116–1127. https://doi.org/10.1021/acsomega.7b00019

Darling, R. S. (1991). An extended equation to calculate NaCl contents from final clathrate melting temperatures in H_2O-CO_2-NaCl fluid inclusions: Implications for P-T isochores location. *Geochimica et Cosmochimica Acta*, *55*(12), 3869–3871. https://doi.org/10.1016/0016-7037(91)90079-k

Diamond, L. W. (1992). Stability of CO_2 clathrate hydrate + CO_2 liquid + CO_2 vapour + aqueous KCl-NaCl solutions: Experimental determination and application to salinity estimates of fluid inclusions. *Geochimica et Cosmochimica Acta*, *56*(1), 273–280. https://doi.org/10.1016/0016-7037(92)90132-3

Diamond, L. W. (2001). Review of the systematics of CO_2-H_2O fluid inclusions. *Lithos*, *55*(1–4), 69–99. https://doi.org/10.1016/s0024-4937(00)00039-6

Diamond, L. W. (2003). Introduction to gas-bearing, aqueous fluid inclusions. In I. Samson, A. Anderson, & M. Marshall (Eds.), *Fluid inclusions: Analysis and interpretation* (Vol. 32, pp. 101–158). Mineralogical Association of Canada Short Course.

Dinel, E., Fowler, A. D., Ayer, J., Still, A., Tylee, K., & Barr, E. (2008). Lithogeochemical and stratigraphic controls on gold mineralization within the metavolcanic rocks of the Hoyle Pond Mine, Timmins, Ontario. *Economic Geology*, *103*(6), 1341–1363. https://doi.org/10.2113/gsecongeo.103.6.1341

Dubé, B., & Gosselin, P. (2007). Greenstone-hosted quartz-carbonate vein deposits. In W. D. Goodfellow (Ed.), *Mineral deposits of Canada: A synthesis of major deposit-types, district metallogeny, the evolution of geological provinces, and exploration methods* (Vol. 5, pp. 49–73). Geological Association of Canada, Mineral Deposits Division, Special Publication.

Dubosq, R., Lawley, C. J. M., Rogowitz, A., Schneider, D. A., & Jackson, S. (2018). Pyrite deformation and connections to gold mobility: Insight from micro-structural analysis and trace element mapping. *Lithos*, *310*, 86–104. https://doi.org/10.1016/j.lithos.2018.03.024

Fougerouse, D., Micklethwaite, S., Ulrich, S., Miller, J., Godel, B., Adams, D. T., & McCuaig, T. C. (2017). Evidence for two stages of mineralization in West Africa's largest gold deposit: Obuasi, Ghana. *Economic Geology*, *112*(1), 3–22. https://doi.org/10.2113/econgeo.112.1.3

Frezzotti, M. L., Tecce, F., & Casagli, A. (2012). Raman spectroscopy for fluid inclusion analysis. *Journal of Geochemical Exploration*, *112*, 1–20. https://doi.org/10.1016/j.gexplo.2011.09.009

Fuchs, S. H. J., Schumann, D., Williams-Jones, A. E., Murray, A. J., Couillard, M., Lagarec, K., et al. (2017). Gold and uranium concentration by interaction of immiscible fluids (hydrothermal and hydrocarbon) in the Carbon Leader Reef, Witwatersrand Supergroup, South Africa. *Precambrian Research*, *293*, 39–55. https://doi.org/10.1016/j.precamres.2017.03.007

Fusswinkel, T., Wagner, T., & Sakellaris, G. (2017). Fluid evolution of the Neoarchean Pampalo orogenic gold deposit (E Finland): Constraints from LA-ICPMS fluid inclusion microanalysis. *Chemical Geology*, *450*, 96–121. https://doi.org/10.1016/j.chemgeo.2016.12.022

Gaboury, D. (2019). Parameters for the formation of orogenic gold deposits. *Applied Earth Science*, *128*(3), 1–10. https://doi.org/10.1080/25726838.2019.1583310

Garrels, R. M., & Christ, C. L. (1965). *Solutions, minerals and equilibria. Ch. 2*. Harper and Row.

Gehrig, M. (1980). *Phasengleichgewichte und pVT-Daten ternärer Mischungen aus Wasser, Kohlendioxid und Natriumchlorid bis 3 kbar und 550°C* Ph.D. dissertation (p. 109). Karlsruhe Institute of Technology.

Gibert, F., Pascal, M. L., & Pichavant, M. (1998). Gold solubility and speciation in hydrothermal solutions: Experimental study of the stability of hydrosulphide complex of gold (AuHS) at 350 to 450 C and 500 bars. *Geochimica et Cosmochimica Acta*, *62*(17), 2931–2947. https://doi.org/10.1016/s0016-7037(98)00209-9

Glasmacher, U. A., Zentilli, M., & Ryan, R. (2003). Nitrogen distribution in Lower Palaeozoic slates/phyllites of the Meguma Supergroup, Nova Scotia, Canada: Implications for Au and Zn–Pb mineralisation and exploration. *Chemical Geology*, *194*(4), 297–329. https://doi.org/10.1016/s0009-2541(02)00322-4

Goldfarb, R. J., Baker, T., Dubé, B., Groves, D. I., Hart, C. J. R., & Gosselin, P. (2005). Distibution, character, and genesis of gold deposits in metamorphic terranes. In *Economic geology 100th anniversary volume* (pp. 407–450).

Goldfarb, R. J., & Groves, D. J. (2015). Orogenic gold: Common or evolving fluid and metal sources. *Lithos*, *2*, 2–26.

Goldstein, R. H. (1986). Reequilibration of fluid inclusions in low-temperature calcium-carbonate cement. *Geology*, *14*(9), 792–795. https://doi.org/10.1130/0091-7613(1986)14<792:rofiil>2.0.co;2

Goldstein, R. H., & Reynolds, T. J. (1994). Fluid inclusion microthermometry 31. In R. H. Goldstein, T. J. Reynolds, & S. Sed (Eds.), *Systematics of fluid inclusions in diagenetic minerals* (pp. 87–122). Geology Short Course.

Gourcerol, B., Kontak, D. J., Petrus, J. A., & Thurston, P. C. (2020). Application of LA ICP-MS analysis of arsenopyrite to gold metallogeny of the Meguma Terrane, Nova Scotia, Canada. *Gondwana Research*, *81*, 265–290. https://doi.org/10.1016/j.gr.2019.11.011

Graves, M. C., & Zentilli, M. (1988). *Geochemical characterization of the Goldenville Formation—Halifax Formation transition zone of the Meguma Group*. Nova Scotia. Geological Survey of Canada. Open File 1829.

Groves, D. I., Goldfarb, R. J., Robert, F., & Hart, C. J. R. (2003). Gold deposits in metamorphic belts: Overview of current understanding, outstanding problems, future research, and exploration significance. *Economic Geology*, *98*, 1–29. https://doi.org/10.2113/gsecongeo.98.1.1

Groves, D. I., Santosh, M., Wang, Q., Zhang, L., & Zhao, H. (2024). The Boring Billion: A key to resolving controversy on ore-fluid source models for orogenic gold deposits? *Mineralium Deposita*, *59*(3), 435–444. https://doi.org/10.1007/s00126-023-01244-1

Guillong, M., Meier, D. L., Allan, M. M., Heinrich, C. A., & Yardley, B. W. D. (2008). Appendix A6: SILLS: A Matlab-based program for the reduction of Laser Ablation ICP–MS data of homogeneous materials and inclusions. *Short Course Series - Mineralogical Association of Canada*, *40*, 328–333. Vancouver B.C.

Hannon, P., Roy, D., & Mosher, G. (2017). *Revised preliminary economic assessment of the dufferin gold deposit*. Resource Capital Gold Corp.

Harris, I. M., & Schenk, P. E. (1975). The Meguma group. *Atlantic Geology*, *11*(1), 25–46. https://doi.org/10.4138/1814

Hastie, E. C. G, Kontak, D. J., & Lafrance, B. (2020). Gold remobilization: Insights from gold deposits in the Archean Swayze greenstone belt, Abitibi subprovince, Canada. *Economic Geology*, *115*(2), 241–277. https://doi.org/10.5382/econgeo.4709

Hastie, E. C. G., Schindler, M., Kontak, D. J., & Lafrance, B. (2021). Transport and coarsening of gold nanoparticles in an orogenic deposit by dissolution–reprecipitation and Ostwald ripening. *Communications Earth & Environment*, *2*(1), 57. https://doi.org/10.1038/s43247-021-00126-6

Heinrich, C. A., & Eadington, P. J. (1986). Thermodynamic predictions of the hydrothermal chemistry of arsenic, and their significance for the paragenetic sequence of some cassiterite-arsenopyrite-base metal sulfide deposits. *Economic Geology*, *81*(3), 511–529. https://doi.org/10.2113/gsecongeo.81.3.511

Heinrich, C. A., Gunther, D., Audétat, A., Ulrich, T., & Frischknecht, R. (1999). Metal fractionation between magmatic brine and vapor, determined by microanalysis of fluid inclusions. *Geology*, *27*(8), 755–758. https://doi.org/10.1130/0091-7613(1999)027<0755:mfbmba>2.3.co;2

Herzog, M., LaFlamme, C., Beaudoin, G., Barré, G., Martin, L., & Savard, D. (2024). Fluid-rock sulfidation reactions control Au-Ag-Te-Bi precipitation in the Val-d'Or orogenic gold vein field (Abitibi subprovince, Canada). *Mineralium Deposita*, *59*(5), 1–26. https://doi.org/10.1007/s00126-024-01247-6

Hicks, R. J., Jamieson, R. A., & Reynolds, P. H. (1999). Detrital and metamorphic ^{40}Ar/^{39}Ar ages from muscovite and whole-rock samples, Meguma Supergroup, southern Nova Scotia. *Canadian Journal of Earth Sciences*, *36*(1), 23–32. https://doi.org/10.1139/e98-081

Horne, R. J., & Culshaw, N. (2001). Flexural-slip folding in the Meguma Group, Nova Scotia, Canada. *Journal of Structural Geology*, *23*(10), 1631–1652. https://doi.org/10.1016/s0191-8141(01)00017-7

Horne, R. J., & Jodrey, M. (2001). Geology of the Dufferin gold deposit (NTS 11D/16), Halifax County. In D. R. MacDonald (Ed.), *Mineral Res Branch, Rpt act 2001* (pp. 51–68). Nova Scotia Department of Natural Resources. Rpt 2002-1.

Horne, R. J., Jodrey, M., & Woodman, K. (2002). Geology of the Dufferin gold deposit, Port Dufferin, Nova Scotia. In *Atlantic Geoscience Society Colloquium and Annual General Meeting, February 2002. Abstracts*.

Hu, S., Evans, K., Craw, D., Rempel, K., & Grice, K. (2017). Resolving the role of carbonaceous material in gold precipitation in metasediment-hosted orogenic gold deposits. *Geology*, *45*(2), 167–170. https://doi.org/10.1130/g38462.1

Huizenga, J. M. (2001). Thermodynamic modelling of C-O-H fluids. *Lithos*, *55*(1–4), 101–114. https://doi.org/10.1016/s0024-4937(00)00040-2

Huizenga, J. M., & Touret, J. L. R. (1999). Fluid inclusions in shear zones: The case of the Umwindsi shear zone in the Harare-Shamva-Bindura greenstone belt, NE Zimbabwe. *European Journal of Mineralogy*, *11*(6), 1079–1090. https://doi.org/10.1127/ejm/11/6/1079

Jamieson, R. A., Hart, G. G., Chapman, G. G., & Tobey, N. W. (2012). The contact aureole of the South Mountain Batholith in Halifax, Nova Scotia: Geology, mineral assemblages, and isograds. *Canadian Journal of Earth Sciences*, *49*(11), 1280–1296. https://doi.org/10.1139/e2012-058

Jehlička, J., Urban, O., & Pokorny, J. (2003). Raman spectroscopy of carbon and solid bitumens in sedimentary and metamorphic rocks. *Spectrochimica Acta, Part A*, *59*(10), 2341–2352. https://doi.org/10.1016/s1386-1425(03)00077-5

Jurisch, S. A., Heim, S., Krooss, B. M., & Littke, R. (2012). Systematics of pyrolytic gas (N_2, CH_4) liberation from sedimentary rocks: Contribution of organic and inorganic rock constituents. *International Journal of Coal Geology*, *89*, 95–107. https://doi.org/10.1016/j.coal.2011.11.004

Kempe, U., Graupner, T., Seltmann, R., de Boorder, H., Dolgopolova, A., & van Emmichoven, M. Z. (2016). The Muruntau gold deposit (Uzbekistan)–a unique ancient hydrothermal system in the southern Tien Shan. *Geoscience Frontiers*, *7*(3), 495–528. https://doi.org/10.1016/j.gsf.2015.09.005

Kendrick, M. A., Honda, M., Walshe, J., & Petersen, K. (2011). Fluid sources and the role of abiogenic-CH_4 in Archean gold mineralization: Constraints from noble gases and halogens. *Precambrian Research*, *189*(3–4), 313–327. https://doi.org/10.1016/j.precamres.2011.07.015

Kerr, M. J., (2024). Dataset for: Auriferous fluid evolution and the role of carbonaceous matter in a saddle-reef Au deposit: Dufferin deposit, Meguma terrane, Nova Scotia, Canada. https://doi.org/10.5683/SP3/JIZXXK

Kerr, M. J., Hanley, J. J., & Kontak, D. J. (2021). Application of bulk fluid volatile chemistry to exploration for metasedimentary rock-hosted orogenic gold deposits: An example from the Meguma terrane, Nova Scotia, Canada. *Journal of Geochemical Exploration*, *226*, 106764. https://doi.org/10.1016/j.gexplo.2021.106764

Kerr, M. J., Hanley, J. J., Kontak, D. J., Morrison, G. G., Petrus, J., Fayek, M., & Zajacz, Z. (2018). Evidence of upgrading of gold tenor in an orogenic quartz-carbonate vein system by late magmatic-hydrothermal fluids at the Madrid Deposit, Hope Bay Greenstone Belt, Nunavut, Canada. *Geochimica et Cosmochimica Acta*, *241*, 180–218. https://doi.org/10.1016/j.gca.2018.08.030

Kontak, D. J., & Archibald, D. A. (2002). ^{40}Ar/^{39}Ar dating of hydrothermal biotite from high-grade gold mineralization, Tangier gold deposit, Nova Scotia, Canada: Further evidence ca. 370 Ma gold metallogeny in the Meguma Terrane. *Economic Geology*, *97*(3), 619–628. https://doi.org/10.2113/gsecongeo.97.3.619

Kontak, D. J., Ham, L. J., & Dunning, G. (2004). U-Pb dating of the Musquodoboit Batholith, southern Nova Scotia: Evidence for a protracted magmatic-hydrothermal event in a Devonian intrusion. *Atlantic Geology*, *40*(2/3), 207–216. https://doi.org/10.4138/1040

Kontak, D. J., & Horne, R. J. (2010). *A multi-stage origin for the Meguma lode gold deposits, Nova Scotia, Canada: A possible global model for slate belt-hosted gold mineralization. Gold metallogeny: India and beyond* (pp. 58–82). Alpha Science International Ltd.

Kontak, D. J., Horne, R. J., & Kyser, K. (2011). An oxygen isotope study of two contrasting orogenic vein gold systems in the Meguma Terrane, Nova Scotia, Canada, with implications for fluid sources and genetic models. *Mineralium Deposita*, *46*(3), 289–304. https://doi.org/10.1007/s00126-011-0332-0

Kontak, D. J., Horne, R. J., Sandeman, H., Archibald, D. A., & Lee, J. K. (1998). ^{40}Ar/^{39}Ar dating of whole-rock slates from auriferous veins in the Meguma Group, Nova Scotia: Evidence for post metamorphic timing of vein formation. *Canadian Journal of Earth Sciences*, *35*(7), 746–761. https://doi.org/10.1139/e98-028

Kontak, D. J., Horne, R. J., & Smith, P. K. (1996). Hydrothermal characterization of the West Gore Sb-Au deposit, Meguma terrane, Nova Scotia, Canada. *Economic Geology*, *91*(7), 1239–1262. https://doi.org/10.2113/gsecongeo.91.7.1239

Kontak, D. J., & Kerrich, R. (1997). An isotopic (C, O, Sr) study of vein quartz and carbonate from Meguma gold deposits, Nova Scotia, Canada. *Economic Geology*, *92*(2), 161–180. https://doi.org/10.2113/gsecongeo.92.2.161

Kontak, D. J., & Kyser, K. (2011). A fluid inclusion and isotopic study of an intrusion-related gold deposit (IRGD) setting in the 380 Ma South Mountain Batholith, Nova Scotia, Canada: Evidence for multiple fluid reservoirs. *Mineralium Deposita*, *46*(4), 337–363. https://doi.org/10.1007/s00126-011-0331-1

Kontak, D. J., & Smith, P. K. (1989). Sulphur isotopic composition of sulphides from the Beaver Dam and other Meguma-Group-hosted gold deposits, Nova Scotia: Implications for genetic models. *Canadian Journal of Earth Sciences*, *26*(8), 1617–1629. https://doi.org/10.1139/e89-138

Kontak, D. J., Smith, P. K., Kerrich, R., & Williams, P. F. (1990). An integrated model for Meguma Group lode gold deposits, Nova Scotia, Canada. *Geology*, *17*, 238–242.

Kontak, D. J., & Tuba, G. (2017). How can fluid inclusion studies better constrain orogenic gold deposit models: Case studies from the Superior Province and Meguma Terrane, Canada. In *SGA Meeting, August 2017, Volume Proceedings of Extended Abstracts*.

Kontak, D. J., Ulrich, T., & Kyser, T. K. (2012). An Integrated Field, Geochemical, Thermometric and LA ICP-MS study of an intrusion-related Au setting: Evidence for fluid mixing and rock dissolution. In *Program with Abstracts, 11th Pan-American Current Research on Fluid Inclusions Conference, Windsor, ON* (pp. 49–50).

Kouketsu, Y., Mizukami, T., Mori, H., Endo, S., Aoya, M., Hara, H., et al. (2014). A new approach to develop the Raman carbonaceous material geothermometer for low-grade metamorphism using peak width. *Island Arc*, *23*(1), 33–50. https://doi.org/10.1111/iar.12057

Lang, J. R., & Baker, T. (2001). Intrusion-related gold systems: The present level of understanding. *Mineralium Deposita*, *36*(6), 477–489. https://doi.org/10.1007/s001260100184

Large, R. R., Bull, S. W., & Maslennikov, V. V. (2011). A carbonaceous sedimentary source-rock model for Carlin-type and orogenic gold deposits. *Economic Geology*, *106*(3), 331–358. https://doi.org/10.2113/econgeo.106.3.331

Large, R. R., Maslennikov, V. V., Robert, F., Danyushevsky, L. V., & Chang, Z. (2007). Multistage sedimentary and metamorphic origin of pyrite and gold in the giant Sukhoi Log deposit, Lena gold province, Russia. *Economic Geology*, *102*(7), 1233–1267. https://doi.org/10.2113/gsecongeo.102.7.1233

Lawley, C. J., Jackson, S., Yang, Z., Davis, W., & Eglington, B. (2017). Tracing the transition of gold from source to sponge to sink. *Economic Geology*, *112*(1), 169–183. https://doi.org/10.2113/econgeo.112.1.169

Li, X. H., Klyukin, Y. I., Steele-MacInnis, M., Fan, H. R., Yang, K. F., & Zoheir, B. (2020). Phase equilibria, thermodynamic properties, and solubility of quartz in saline-aqueous-carbonic fluids: Application to orogenic and intrusion-related gold deposits. *Geochimica et Cosmochimica Acta*, *283*, 201–221. https://doi.org/10.1016/j.gca.2020.06.008

Liu, D., Xiao, X., Tian, H., Min, Y., Zhou, Q., Cheng, P., & Shen, J. (2013). Sample maturation calculated using Raman spectroscopic parameters for solid organics: Methodology and geological applications. *Chinese Science Bulletin*, *58*(11), 1285–1298. https://doi.org/10.1007/s11434-012-5535-y

Mair, J. L., Goldfarb, R. J., Johnson, C. A., Hart, C. J., & Marsh, E. E. (2006). Geochemical constraints on the genesis of the Scheelite Dome intrusion-related gold deposit, Tombstone gold belt, Yukon, Canada. *Economic Geology*, *101*(3), 523–553. https://doi.org/10.2113/gsecongeo.101.3.523

Malcolm, W. (1929). In *Gold fields of Nova Scotia* (Vol. 156, p. 253). Geological Survey of Canada.

Mao, W., Rusk, B., Yang, F., & Zhang, M. (2017). Physical and chemical evolution of the Dabaoshan porphyry Mo deposit, South China: Insights from fluid inclusions, cathodoluminescence, and trace elements in quartz. *Economic Geology*, *112*(4), 889–918. https://doi.org/10.2113/econgeo.112.4.889

Marsala, A., Wagner, T., & Wälle, M. (2013). Late-metamorphic veins record deep ingression of meteoric water: A LA-ICPMS fluid inclusion study from the fold-and-thrust belt of the Rhenish Massif, Germany. *Chemical Geology*, *351*, 134–153. https://doi.org/10.1016/j.chemgeo.2013.05.008

Marsh, E. E., Goldfarb, R. J., Hart, C. J., & Johnson, C. A. (2003). Geology and geochemistry of the Clear Creek intrusion-related gold occurrences, Tintina Gold Province, Yukon, Canada. *Canadian Journal of Earth Sciences*, *40*(5), 681–699. https://doi.org/10.1139/e03-018

Massonne, H. J., Clarke, D. B., & MacDonald, M. A. (2010). Intrusion level of the Musquodoboit Batholith in Nova Scotia, Canada–a case study. *Zeitschrift für Geologische Wissenschaften*, *38*, 181–194.

Matthäi, S. K., Henley, R. W., & Heinrich, C. A. (1995). Gold precipitation by fluid mixing in bedding-parallel fractures near carbonaceous slates at the Cosmopolitan Howley gold deposit, northern Australia. *Economic Geology*, *90*(8), 2123–2142. https://doi.org/10.2113/gsecongeo.90.8.2123

McCuaig, T. C., & Kerrich, R. (1998). P-T-t-deformation-fluid characteristics of lode gold deposits: Evidence from alteration systematics. *Ore Geology Reviews*, *12*(6), 381–453. https://doi.org/10.1016/s0169-1368(98)80002-4

McLeish, D. F., Williams-Jones, A. E., Vasyukova, O. V., Clark, J. R., & Board, W. S. (2021). Colloidal transport and flocculation are the cause of the hyperenrichment of gold in nature. *Proceedings of the National Academy of Sciences of the United States of America*, *118*(20), e2100689118. https://doi.org/10.1073/pnas.2100689118

McNaughton, N. J., Barley, M. E., Cassidy, K. F., Golding, S. D., Groves, D. I., Ho, S. E., et al. (1990). Carbon isotope studies. In S. E. Ho & J. M. Bennett (Eds.), *Gold deposits of the Archaean Yilgarn Block, Western Australia: Nature, genesis and exploration guides* (Vol. 20). Geology Key Centre & University Extension, University of Western Australia.

Miller, J. D., Wan, R. Y., & Diaz, X. (2005). Preg-robbing gold ores. In *Developments in mineral processing* (Vol. 15, pp. 937–972). https://doi.org/10.1016/s0167-4528(05)15038-8

Miron, G. D., Wagner, T., Wälle, M., & Heinrich, C. A. (2013). Major and trace-element composition and pressure–temperature evolution of rock-buffered fluids in low-grade accretionary-wedge metasediments, Central Alps. *Contributions to Mineralogy and Petrology*, *165*(5), 981–1008. https://doi.org/10.1007/s00410-012-0844-3

Monecke, T., Monecke, J., & Reynolds, T. J. (2019). The influence of CO2 on the solubility of quartz in single-phase hydrothermal fluids: Implications for the formation of stockwork veins in porphyry copper deposits. *Economic Geology*, *114*(6), 1195–1206. https://doi.org/10.5382/econgeo.4680

Monecke, T., Monecke, J., Reynolds, T. J., Tsuruoka, S., Bennett, M. M., Skewes, W. B., & Palin, R. M. (2018). Quartz solubility in the H$_2$O-NaCl system: A framework for understanding vein formation in porphyry copper deposits. *Economic Geology*, *113*(5), 1007–1046. https://doi.org/10.5382/econgeo.2018.4580

Morelli, R. M., Creaser, R., Selby, D., Kontak, D. J., & Horne, R. J. (2005). Rhenium-Osmium geochronology of arsenopyrite in Meguma Group gold deposits, Meguma Terrane, Nova Scotia, Canada: Evidence for multiple gold-mineralizing events. *Economic Geology*, *100*(6), 1229–1242. https://doi.org/10.2113/100.6.1229

Murphy, J. B., Waldron, J. W., Kontak, D. J., Pe-Piper, G., & Piper, D. J. (2011). Minas Fault Zone: Late Paleozoic history of an intra-continental orogenic transform fault in the Canadian Appalachians. *Journal of Structural Geology*, *33*(3), 312–328. https://doi.org/10.1016/j.jsg.2010.11.012

Naden, J., & Shepherd, T. J. (1989). Role of methane and carbon dioxide in gold deposition. *Nature*, *342*(6251), 793–795. https://doi.org/10.1038/342793a0

Neumayr, P., & Hagemann, S. G. (2002). Hydrothermal fluid evolution within the Cadillac tectonic zone, Abitibi greenstone belt, Canada: Relationship to auriferous fluids in adjacent second-and third-order shear zones. *Economic Geology*, *97*(6), 1203–1225. https://doi.org/10.2113/gsecongeo.97.6.1203

Neyedley, K., Hanley, J. J., Fayek, M., & Kontak, D. J. (2017). Textural, fluid inclusion, and stable oxygen isotope constraints on vein formation and gold precipitation at the 007 deposit, Rice Lake Greenstone Belt, Bissett, Manitoba, Canada. *Economic Geology*, *112*(3), 629–660. https://doi.org/10.2113/econgeo.112.3.629

Oberthür, T., Mumm, A. S., Vetter, U., Simon, K., & Amanor, J. A. (1996). Gold mineralization in the Ashanti Belt of Ghana; genetic constraints of the stable isotope geochemistry. *Economic Geology*, *91*(2), 289–301. https://doi.org/10.2113/gsecongeo.91.2.289

O'Day, P. A. (2006). Chemistry and mineralogy of arsenic. *Elements*, *2*(2), 77–83. https://doi.org/10.2113/gselements.2.2.77

Olivo, G. R., & Williams-Jones, A. E. (2002). Genesis of the auriferous C quartz-tourmaline vein of the Siscoe mine, Val d'Or district, Abitibi subprovince, Canada: Structural, mineralogical and fluid inclusion constraints. *Economic Geology*, *97*(5), 929–947. https://doi.org/10.2113/97.5.929

Oszczepalski, S., Speczik, S., & Wojciechowski, A. (2011). Gold mineralization in the Kupferschiefer oxidized series of the North Sudetic trough, SW Poland. In *Gold in Poland* (pp. 153–168). AM Momograph 2.

Padgham, W. A. (1986). Turbidite-Hosted Gold–Quartz Veins in the Slave structural Province, NWT. In J. D. Keppie, R. W. Boyle, & S. J. Haynes (Eds.), *Turbidite-Hosted Gold Deposits: Geologic Association of Canada, Special Paper* (Vol. 32, pp. 119–134).

Papineau, D. M. S. J., Mojzsis, S. J., Karhu, J. A., & Marty, B. (2005). Nitrogen isotopic composition of ammoniated phyllosilicates: Case studies from Precambrian metamorphosed sedimentary rocks. *Chemical Geology*, *216*(1–2), 37–58. https://doi.org/10.1016/j.chemgeo.2004.10.009

Parnell, J. (1996). Phanerozoic analogues for carbonaceous matter in Witwatersrand ore deposits. *Economic Geology*, *91*(1), 55–62. https://doi.org/10.2113/gsecongeo.91.1.55

Phillips, G. N., & Evans, K. A. (2004). Role of CO_2 in the formation of gold deposits. *Nature*, *429*(6994), 860–863. https://doi.org/10.1038/nature02644

Pitcairn, I. K., Roberts, S., Teagle, D. A., & Craw, D. (2005). Detecting hydrothermal graphite deposition during metamorphism and gold mineralization. *Journal of the Geological Society*, *162*(3), 429–432. https://doi.org/10.1144/0016-764904-139

Pitcairn, I. K., Teagle, D. A., Craw, D., Olivo, G. R., Kerrich, R., & Brewer, T. S. (2006). Sources of metals and fluids in orogenic gold deposits: Insights from the Otago and Alpine Schists, New Zealand. *Economic Geology*, *101*(8), 1525–1546. https://doi.org/10.2113/gsecongeo.101.8.1525

Radtke, A. S., & Scheiner, B. J. (1970). Studies of hydrothermal gold deposition (I). Carlin gold deposit, Nevada: The role of carbonaceous materials in gold deposition. *Economic Geology*, *65*(2), 87–102. https://doi.org/10.2113/gsecongeo.65.2.87

Rauchenstein-Martinek, K., Wagner, T., Wälle, M., & Heinrich, C. A. (2014). Gold concentrations in metamorphic fluids: A LA-ICPMS study of fluid inclusions from the Alpine orogenic belt. *Chemical Geology*, *385*, 70–83. https://doi.org/10.1016/j.chemgeo.2014.07.018

Rauchenstein-Martinek, K., Wagner, T., Wälle, M., Heinrich, C. A., & Arlt, T. (2016). Chemical evolution of metamorphic fluids in the Central Alps, Switzerland: Insight from LA-ICPMS analysis of fluid inclusions. *Geofluids*, *16*(5), 877–908. https://doi.org/10.1111/gfl.12194

Razvozzhaeva, E. A., Prokof'ev, V. Y., Spiridonov, A. M., Kh, M. D., & Prokopchuk, S. I. (2002). Precious metals and carbonaceous substance in ores of the Sukhoi Log deposit (Eastern Siberia, Russia).

Reed, M., Rusk, B., & Palandri, J. (2013). The Butte magmatic-hydrothermal system: One fluid yields all alteration and veins. *Economic Geology*, *108*(6), 1379–1396. https://doi.org/10.2113/econgeo.108.6.1379

Renders, P. J., & Seward, T. M. (1989). The stability of hydrosulphido- and sulphido-complexes of Au(I) and Ag(I) at 25°C. *Geochimica et Cosmochimica Acta*, *53*(2), 245–253. https://doi.org/10.1016/0016-7037(89)90377-3

Ridley, J. B., & Diamond, L. W. (2000). Fluid chemistry of orogenic lode gold deposits and implications for genetic models. *Society of Economic Geology Reviews*, *13*, 141–162.

Ridley, J. B., & Hagemann, S. G. (1999). Interpretation of post-entrapment fluid-inclusion re-equilibration at the Three Mile Hill, Marvel Loch and Griffins Find high-temperature lode-gold deposits, Yilgarn Craton, Western Australia. *Chemical Geology*, *154*(1–4), 257–278. https://doi.org/10.1016/s0009-2541(98)00135-1

Roedder, E. (1984). Fluid inclusions. *Reviews in Mineralogy*, *12*, 644.

Rosso, K. M., & Bodnar, R. J. (1995). Microthermometric and Raman spectroscopic detection limits of CO_2 in fluid inclusions and the Raman spectroscopic characterization of CO_2. *Geochimica et Cosmochimica Acta*, *59*(19), 3961–3975. https://doi.org/10.1016/0016-7037(95)94441-h

Rusk, B., Reed, M., Bignall, G., & Tsuchiya, N. (2004). Natural and synthetic quartz growth and dissolution revealed by scanning electron microscope cathodoluminescence. In *14th International Conference on the Properties of Water and Steam*. Kyoto.

Rusk, B. G., Reed, M. H., Dilles, J. H., Klemm, L. M., & Heinrich, C. A. (2004). Compositions of magmatic hydrothermal fluids determined by LA-ICP-MS of fluid inclusions from the porphyry copper–molybdenum deposit at Butte, MT. *Chemical Geology*, *210*(1–4), 173–199. https://doi.org/10.1016/j.chemgeo.2004.06.011

Ryan, R. J., & Smith, P. K. (1998). A review of the mesothermal gold deposits of the Meguma Group, Nova Scotia, Canada. *Ore Geology Reviews*, *13*(1–5), 153–183. https://doi.org/10.1016/s0169-1368(97)00017-6

Sangster, A. L. (1992). Light stable isotope evidence for a metamorphogenic origin for bedding-parallel, gold-bearing veins in the Cambrian flysch, Meguma Group, Nova Scotia. *Exploration And Mining Geology*, *1*, 69–79.

Sangster, A. L., & Smith, P. K. (2007). Metallogenic summary of the Meguma gold deposits, Nova Scotia. In W. D. Goodfellow (Ed.), *Mineral deposits of Canada: A synthesis of major deposit-types, district metallogeny, the evolution of geological provinces, and exploration methods* (Vol. 5, pp. 723–732). Geological Association of Canada, Mineral Deposits Division, Special Publication.

Scheiner, B. J. (1971). Processing refractory carbonaceous ores for gold recovery. *Journal of the Minerals Metals & Materials Society*, *23*(3), 37–40. https://doi.org/10.1007/bf03355688

Schmidt, C., & Bodnar, R. J. (2000). Synthetic fluid inclusions: XVI. PVTX properties in the system H_2O-NaCl-CO_2 at elevated temperatures, pressures, and salinities. *Geochimica et Cosmochimica Acta*, *64*(22), 3853–3869. https://doi.org/10.1016/s0016-7037(00)00471-3

Seo, J. H., Guillong, M., Aerts, M., Zajacz, Z., & Heinrich, C. A. (2011). Microanalysis of S, Cl, and Br in fluid inclusions by LA-ICP-MS. *Chemical Geology*, *284*, 35–44. https://doi.org/10.1016/j.chemgeo.2011.02.003

Seward, T. M. (1973). Thio complexes of gold and the transport of gold in hydrothermal ore solutions. *Geochimica et Cosmochimica Acta*, *37*(3), 379–399. https://doi.org/10.1016/0016-7037(73)90207-x

Shelton, K. L., McMenamy, T. A., Van Hees, E. H. P., & Falck, H. (2004). Deciphering the complex fluid history of a greenstone-hosted gold deposit: Fluid inclusion and stable isotope studies of the Giant mine, Yellowknife, Northwest Territories, Canada. *Economic Geology*, *99*, 1643–1663.

Shenberger, D., & Barnes, H. L. (1989). Solubility of gold in aqueous sulfide solutions from 150 to 350°C. *Geochimica et Cosmochimica Acta*, *53*(2), 269–278. https://doi.org/10.1016/0016-7037(89)90379-7

Sherman, D. M., Ragnarsdottir, K. V., & Oelkers, E. H. (2000). Antimony transport in hydrothermal solutions: An EXAFS study of antimony (V) complexation in alkaline sulfide and sulfide–chloride brines at temperatures from 25 C to 300 C at Psat. *Chemical Geology*, *167*(1–2), 161–167. https://doi.org/10.1016/s0009-2541(99)00207-7

Sibson, R. H., Robert, F., & Poulsen, K. H. (1988). High-angle reverse faults, fluid-pressure cycling, and mesothermal gold-quartz deposits. *Geology*, *16*(6), 551–555. https://doi.org/10.1130/0091-7613(1988)016<0551:harffp>2.3.co;2

Steadman, J. A., Large, R. R., Meffre, S., & Bull, S. W. (2013). Age, origin and significance of nodular sulfides in 2680 Ma carbonaceous black shale of the Eastern Goldfields Superterrane, Yilgarn Craton, Western Australia. *Precambrian Research*, *230*, 227–247. https://doi.org/10.1016/j.precamres.2013.02.013

Steele-MacInnis, M., Han, L., Lowell, R. P., Rimstidt, J. D., & Bodnar, R. J. (2012). The role of fluid phase immiscibility in quartz dissolution and precipitation in sub-seafloor hydrothermal systems. *Earth and Planetary Science Letters*, *321*, 139–151. https://doi.org/10.1016/j.epsl.2011.12.037

Stefánsson, A., & Seward, T. M. (2004). Gold (I) complexing in aqueous sulphide solutions to 500 C at 500 bar. *Geochimica et Cosmochimica Acta*, *68*(20), 4121–4143. https://doi.org/10.1016/j.gca.2004.04.006

Sun, M., Monecke, T., Reynolds, T. J., & Yang, Z. (2020). Understanding the evolution of magmatic-hydrothermal systems based on micro-textural relationships, fluid inclusion petrography, and quartz solubility constraints: Insights into the formation of the Yulong Cu-Mo porphyry deposit, eastern Tibetan Plateau, China. *Mineralium Deposita*, *56*(5), 1–20. https://doi.org/10.1007/s00126-020-01003-6

Tan, H., Feng, D., van Deventer, J. S. J., & Lukey, G. C. (2005). Effect of contaminant carbonaceous matter on the sorption of gold by pyrite. *International Journal of Mineral Processing*, *76*(1), 244–259. https://doi.org/10.1016/j.minpro.2005.02.006

Thompson, J. F. H., Sillitoe, R. H., Baker, T., Lang, J. R., & Mortensen, J. K. (1999). Intrusion-related gold deposits associated with tungsten-tin provinces. *Mineralium Deposita*, *34*(4), 323–334. https://doi.org/10.1007/s001260050207

Touret, J. L. R. (1981). Fluid inclusions in high grade metamorphic rocks. In L. S. Hollister & M. L. Crawford (Eds.), *Short course in fluid inclusions: Applications to petrology* (Vol. 6, pp. 182–208). Mineralogical Association of Canada Short Course.

Tuba, G., Kontak, D. J., Choquette, B. G., Pfister, J., Hastie, E. C., & van Hees, E. H. (2021). Fluid diversity in the gold-endowed Archean orogenic systems of the Abitibi greenstone belt (Canada) I: Constraining the PTX of prolonged hydrothermal systems. *Ore Geology Reviews*, *135*, 104221. https://doi.org/10.1016/j.oregeorev.2021.104221

Ulmer, P., & Luth, R. W. (1991). The graphite-COH fluid equilibrium in P, T, fO_2 space: An experimental determination to 30 kbar and 1600°C. *Contributions to Mineralogy and Petrology*, *106*(3), 265–272. https://doi.org/10.1007/bf00324556

Upton, P., & Craw, D. (2008). Modelling the role of graphite in development of a mineralised mid-crustal shear zone, Macraes mine, New Zealand. *Earth and Planetary Science Letters*, *266*(3–4), 245–255. https://doi.org/10.1016/j.epsl.2007.10.048

Van den Kerkhof, A. M., & Hein, U. F. (2001). Fluid inclusion petrography. *Lithos*, *55*(1–4), 27–47. https://doi.org/10.1016/s0024-4937(00)00037-2

van Deventer, J. S. J., Tan, H., Feng, D., & Lukey, G. C. (2005). The behavior of carbonaceous matter in gold extraction. In G. Deschenes, D. Hodouin, & L. Lorenzen (Eds.), *Proceedings, Treatment of Gold Ores, 44th Annual Conference of Metallurgists of CIM* (p. 111e125).

van Hees, E. H., Shelton, K. L., McMenamy, T. A., Ross Jr, L. M., Cousens, B. L., Falck, H., et al. (1999). Metasedimentary influence on metavolcanic-rock–hosted greenstone gold deposits: Geochemistry of the Giant mine, Yellowknife, Northwest Territories, Canada. *Geology*, *27*(1), 71–74. https://doi.org/10.1130/0091-7613(1999)027<0071:miomrh>2.3.co;2

Van Staal, C. R. (2007). Pre-Carboniferous tectonic evolution and metallogeny of the Canadian Appalachians. In W. D. Goodfellow (Ed.), *Mineral deposits of Canada: A synthesis of major deposit-types, district metallogeny, the evolution of geological provinces, and exploration methods* (Vol. 5, pp. 793–818). Geological Association of Canada, Mineral Deposits Division, Special Publication.

Vaughan, J. P. (2004). The process mineralogy of gold: The classification of ore types. *Journal of the Minerals Metals & Materials Society*, *56*(7), 46–48. https://doi.org/10.1007/s11837-004-0092-8

Vilor, N. V. (1983). Gold in black shales. *Geochemistry International*, *20*, 167–177.

Voisey, C. R., Maas, R., Tomkins, A. G., Brauns, M., & Brügmann, G. (2019). Extreme silver isotope variation in orogenic gold systems implies multistaged metal remobilization during ore genesis. *Economic Geology*, *114*(2), 233–242. https://doi.org/10.5382/econgeo.2019.4629

Waldron, J. W. (1992). The Goldenville–Halifax transition, Mahone Bay, Nova Scotia: Relative sea-level rise in the Meguma source terrane. *Canadian Journal of Earth Sciences*, *29*(5), 1091–1105. https://doi.org/10.1139/e92-087

White, C. E., & Goodwin, T. A. (2011). Lithogeochemistry, petrology, and the acid-generating potential of the Goldenville and Halifax groups and associated granitoid rocks in metropolitan Halifax Regional Municipality, Nova Scotia, Canada. *Atlantic Geology*, *47*, 158–184. https://doi.org/10.4138/atlgeol.2011.008

White, C. E., Palacios, T., Jensen, S., & Barr, S. M. (2012). Cambrian–ordovician acritarchs in the Meguma terrane, Nova Scotia, Canada: Resolution of early Paleozoic stratigraphy and implications for paleogeography. *GSA Bulletin*, *124*(11–12), 1773–1792. https://doi.org/10.1130/b30638.1

Williams-Jones, A. E., Bowell, R. J., & Migdisov, A. A. (2009). Gold in solution. *Elements*, *5*, 281–287. https://doi.org/10.2113/gselements.5.5.281

Williams-Jones, A. E., & Heinrich, C. A. (2005). 100th Anniversary special paper: Vapor transport of metals and the formation of magmatic-hydrothermal ore deposits. *Economic Geology*, *100*(7), 1287–1312. https://doi.org/10.2113/gsecongeo.100.7.1287

Wood, S. A., & Samson, I. M. (1998). Solubility of ore minerals and complexation of ore metals in hydrothermal solutions. In *Reviews in economic geology* (pp. 33–80). Society of Economic Geologists.

Xing, Y., Brugger, J., Tomkins, A., & Shvarov, Y. (2019). Arsenic evolution as a tool for understanding formation of pyritic gold ores. *Geology*, *47*(4), 335–338. https://doi.org/10.1130/g45708.1

Zoheir, B., Steele-MacInnis, M., & Garbe-Schönberg, D. (2019). Orogenic gold formation in an evolving, decompressing hydrothermal system: Genesis of the Samut gold deposit, Eastern Desert, Egypt. *Ore Geology Reviews*, *105*, 236–257. https://doi.org/10.1016/j.oregeorev.2018.12.030